Naval Research Laboratory

Washington, DC 20375-5320

NRL/MR/6003--18-9815

A Coherent Structure Dynamics Model for Non-Equilibrium Turbulence

Jay Boris

Chief Scientist
Material Science and Component Technology Directorate

September 14, 2018

REPORT DOCUMENTATION PAGE

Form Approved
OMB No. 0704-0188

1. REPORT DATE *(DD-MM-YYYY)*	**2. REPORT TYPE**	**3. DATES COVERED** *(From - To)*
14-09-2018	Memorandum Report	

4. TITLE AND SUBTITLE

A Coherent Structure Dynamics Model for Non-Equilibrium Turbulence

5a. CONTRACT NUMBER

5b. GRANT NUMBER
64-4464-0-8-5

5c. PROGRAM ELEMENT NUMBER

6. AUTHOR(S)

Jay Boris

5d. PROJECT NUMBER

5e. TASK NUMBER

5f. WORK UNIT NUMBER

7. PERFORMING ORGANIZATION NAME(S) AND ADDRESS(ES)

Naval Research Laboratory
4555 Overlook Avenue, SW
Washington, DC 20375

8. PERFORMING ORGANIZATION REPORT NUMBER

NRL/MR/6003--18-9815

9. SPONSORING / MONITORING AGENCY NAME(S) AND ADDRESS(ES)

10. SPONSOR / MONITOR'S ACRONYM(S)

11. SPONSOR / MONITOR'S REPORT NUMBER(S)

12. DISTRIBUTION / AVAILABILITY STATEMENT

DISTRIBUTION STATEMENT A; Approved for public release; distribution is unlimited.

13. SUPPLEMENTARY NOTES

14. ABSTRACT

See Report

15. SUBJECT TERMS

Computational Fluid Dynamics, Coherent Structure Dynamics, Turbulent Spectrum, Kinetic Energy, Rotor Number Density, Equations, Scales

16. SECURITY CLASSIFICATION OF:			**17. LIMITATION OF ABSTRACT**	**18. NUMBER OF PAGES**	**19a. NAME OF RESPONSIBLE PERSON**
					Jay Boris
a. REPORT	**b. ABSTRACT**	**c. THIS PAGE**	Unclassified Unlimited	34	**19b. TELEPHONE NUMBER** *(include area code)*
Unclassified Unlimited	Unclassified Unlimited	Unclassified Unlimited			(202) 767-3055

Standard Form 298 (Rev. 8-98)
Prescribed by ANSI Std. Z39.18

This page intentionally left blank.

A Coherent Structure Dynamics Model for Non-Equilibrium Turbulence

Jay Boris, U.S. Naval Research Laboratory

Abstract:

This paper introduces a computational model that computes the time-dependent evolution of a non-equilibrium turbulence spectrum from the system size down to the viscous dissipation scale. Turbulence models for use with Computational Fluid Dynamics (CFD) have at best treated the inertial-range below the CFD resolution as if obeying a renormalizable or scale-similar equilibrium described by the Kolmogorov spectrum with a spectral energy density that scales as $k^{-5/3}$. The "Coherent Structure Dynamics" (CSD) model introduced here addresses situations where the time-scale for changes in the macroscopic fluid dynamics is short and thus the resulting turbulence is far from an equilibrium cascade because the turbulent small scales that drive the dissipation will not have had time to equilibrate. Such circumstances can be caused, for example, by strong shocks passing through passive density gradients or fuel injection into supersonic flows. Mixing on the molecular scale and thus chemical reactions will be delayed until the short scales in the velocity spectrum are energized.

The CSD model is not derived from the Navier-Stokes equations. It is constructed to satisfy the important physical conditions of the problem including scale consistency of the inviscid, nonlinear, fluid-dynamic interactions between the coherent structures that actually comprise turbulence. In addition to treating the kinetic energy density as a function of scale size down to the Kolmogorov dissipation scale, a number density of coherent structures at each scale is introduced to account for the fact that the relative spacing of the structures comprising turbulence, particularly away from equilibrium, may not be the same at all scales. This dynamic system relaxes to the Kolmogorov spectrum with a definite pre-dissipative bump (the bottleneck). Two scale-independent parameters in the model are calibrated using the Taylor-Green vortex problem. Examples are presented and tests of the model are discussed.

Manuscript approved September 14, 2018.

Glossary:

ρ mass density of the fluid (gm/cc).

ν Kinematic viscosity of the fluid (gm/(sec cm)).

L_{sys} System scale length, 10 m in examples following.

R_k Length scale (cm) of the rotors in scale size bin *k*.

The following variables change in time due to the stiff evolution equations . . .

E_k Energy density (ergs/cc) of rotors of size R_k ($k = 0, kmax$).

N_k Number density of rotors (#/cc) of scale size R_k.

ε_k Energy in a single rotor of size R_k. $\varepsilon_k = 3\pi\rho R_k^3 V_k^2 = E_k/N_k$

The following derived quantities are also used . . .

P_k^f Packing fraction for rotors of size R_k (dimensionless).

$P_k^f \equiv 3\pi R_k^3 N_k$. Thus $E_k \equiv 3\pi\rho R_k^3 V_k^2 N_k = \rho P_k^f V_k^2$

P_k Packing fraction temporary. $P_k \equiv (P_k^f)^{2/3} = (3\pi R_k^3 N_k)^{2/3}$

V_k Characteristic average velocity (energy weighted) of rotors of size R_k.

$$V_k \equiv \sqrt{E_k/(\rho P_k^f)}$$

S_k Typical separation distance (cm) of rotors of size R_k.

$$\frac{4\pi}{3} S_k^3 N_k = 1 \rightarrow S_k \equiv R_k/\left[P_k^f\right]^{1/3}$$

V_k^{pre} Rotor precession velocity, $V_k^{pre} \equiv V_k R_k/S_k$, decreases with separation

τ_k Interaction time (sec) of rotors of size R_k with each other. $\tau_k = 2\pi S_k/V_k^{pre}$

1. Introduction

This paper introduces a computational model that computes the time-dependent evolution of a non-equilibrium turbulent spectrum from the system size down to the viscous dissipation scale. Turbulence models for use with Computational Fluid Dynamics (CFD) have generally treated the inertial-range below the CFD resolution as if obeying a renormalizable [Yakhot and Orszag, 1986] or scale-similar equilibrium described by the Kolmogorov spectrum with a spectral energy density that scales as $k^{-5/3}$. The "Coherent Structure Dynamics" (CSD) model introduced here addresses situations where the time-scale for changes in the macroscopic fluid dynamics is short and thus the resulting turbulence can be far from an equilibrium cascade because the turbulent small scales that drive the dissipation will not have had time to equilibrate. Such circumstances can be caused, for example, by strong shocks passing through passive density gradients (Boris & Picone, 1980; Picone, et al., 1981,1984; Grinstein, et al., 2018), or combustion in supersonic flows (Goodwin and Oran, 2018) or rapid, energy-releasing chemical reactions in nearby pockets of previously mixed fluid (Hamlington, et al., 2011; Gamezo, et al., 2014; Poludnenko, 2015, Towery, et al., 2016). When the small scales in the turbulence spectrum have too little energy, it often means that mixing has not yet occurred on the molecular scale and thus chemical reactions will be delayed.

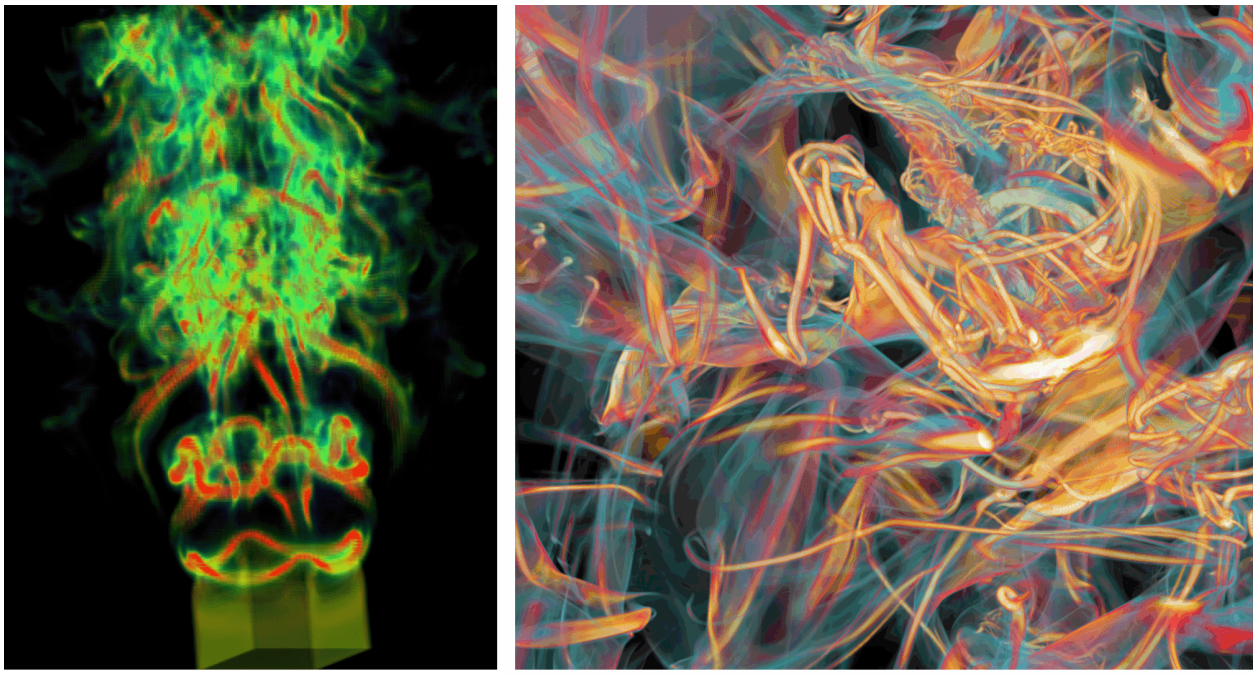

Grinstein, LANL - FCT **Woodward, et al. Minnesota - PPM**

Figure 1.1 Illustrates detailed numerical simulations of the small-scale structure of turbulent flows. Left: a simulation of flow structure in a square jet using Flux-Corrected Transport (FCT) performed by Fernando F. Grinstein, now at LANL. Right: A simulation of compressible turbulence in a periodic box using the Piecewise Parabolic Method (PPM) courtesy of Paul Woodard and colleagues at the University of Minnesota.

The CSD model is based on the time-dependent nonlinear fluid-dynamic interaction of the "coherent structures" that actually comprise turbulence (Brown & Roshko, 1974). Figure 1.1 presents two flow visualizations from detailed large-eddy simulations (LES) approximating high Reynolds-Number flow conditions. The panel on the left above is a rendering of the vorticity in a spatially evolving square jet (Grinstein, 2001) and the panel on the right is vorticity magnitude observed during turbulence decay in a triply periodic box. This latter case is the idealized system often treated in high-resolution Direct Numerical Simulation (DNS) (e.g. Moin and Mahesh,1998; Moser, et al., 1999; A. Kajzer, et al.,2014). The resolution possible in today's simulations, though greater than the pace-setting computations in Fig. 1.1, is still far from adequate to treat airflow on an urban scale and yet resolve the strong, intermittent eddies on scales of five to ten centimeters that will affect small UAVs and drones. The turbulence below the macroscopic scales is dominated by filamentary vortex structures, as seen above. Brown and Roshko observed the same behavior in experiments, calling these filaments "coherent structures." They distinguished between these coherent structures and the view of turbulence as a mishmash of small scale random flows as had previous been thought. The model being described here evolves these coherent structures throughout the inertial range and down into the dissipation range and thus has been named Coherent Structure Dynamics (CSD).

In Fig. 1.1 the coherent structures appear as relatively isolated filaments whereas the larger scales do not appear to show correspondingly coherent, or at least visible, structures. Vortex dynamics models, pursued for decades for vortex filament problems like this, are deterministic and Lagrangian in representation. They are based on solving the motion of vortex filaments composed of a number of line segments or spherical vortex cores coupled by velocities that can be computed from the Biot-Savart law, e.g. Knio and Ghoneim (1990) or Pullin and Saffman (1998). Only one

realization of the complex flow field is computed at a time and the computational cost for this one realization becomes prohibitive when multiscale complexity in the flow approaching turbulence is considered. Here I am describing a more statistical treatment of the interaction and dynamics of these coherent structures to expose important, more generic behaviors. Therefore, CSD, by itself, does not seek to compute one particular deterministic turbulent realization, but rather expresses the coupling of turbulent kinetic energy between the different spatial scales comprising the turbulence. The determination of specific realizations will be determined after CSD has calculated the non-equilibrium, time-varying energy spectrum from which spatial and temporal correlated realizations must be drawn.

The CSD model is not derived from the Navier-Stokes equations. It is constructed to satisfy the important physical requirements of the problem including inviscid kinetic energy conservation, scale consistency of the inviscid, nonlinear, fluid-dynamic interactions between the coherent structures that actually power turbulent cascade, and properly scaled viscous damping acting at all scales (Sections 2 and 3). Because the nonlinear interactions between adjacent scales in the spectrum are all represented identically, the spectrum can be resolved far beyond where CFD has the ability to resolve. In addition to treating the kinetic energy density as a function of scale size down to the Kolmogorov dissipation length, a number density of coherent structures at each scale has been introduced to account for the fact that the relative spacing of the coherent structures, particularly away from equilibrium, will not be the same at all scales Section 3). This number density is coupled to the energy spectrum but evolves according to a different equation set.

The coupled CSD system of kinetic energy densities and number densities relaxes to the Kolmogorov spectrum with a definite pre-dissipative bump, also called the bottleneck. The two scale-independent parameters governing cascade in the CSD model are calibrated using the Taylor-Green vortex problem (Section. Examples are presented and tests of the model are discussed.

The coupling of energy between turbulent scales has been studied extensively in the Fourier viewpoint e.g., (Brasseur and Corrsin, 1987; Brasseur, 1991; Brasseur and Wei, 1994). Triads of wavelengths interact nonlinearly to move energy to longer and shorter wavelength. This Fourier-based approach is mathematically tractable and yields some insights but essentially ignores the coherent structures known to make up a turbulent flow. It certainly does not provide an efficient way to approximate the small-scale, time-dependent flows that will buffet a small UAV.

2. The Coherent Structure Dynamics Model

The coupling of energy between adjacent wavelength scales is treated here by computing energy-conserving fluid dynamic interactions between short segments of the filamentary coherent structures which I will call rotors. These rotor interactions are not integrated deterministically as done in vortex dynamics but the energy transfer between rotors in adjacent scale-size bins is treated statistically by integrating a set of coupled ordinary different equations for the summed energy density and average number density of the rotors at each of a number of discrete scales. These different scales are distributed logarithmically so turbulent cascade can be approximated over many orders of magnitude. Energy conservation is enforced in detail and the required scale-similarity in the behavior of the rotor interactions at different scales is maintained.

The rotor sizes in the CSD model are assumed discretized into bins separated by a factor of two in size. This allows us to represent the spectrum down to the dissipation scale with a few tens of bins and independent variables. It also allows a particularly simple representation of the coherent-structure interactions. The grid in wave number, or scale space, used to represent the rotor sizes is shown schematically in Figure 2.1 below. The red lines in each size bin above show

a decreasing energy density E_k on a log-log scale and the brown lines show an increasing rotor number density N_k. This compact representation provides a fast evaluation of the evolving non-equilibrium turbulence spectrum that can be evaluated at a number of separate locations in space. This speed will be used to estimate the high-resolution turbulence, for example, within a number of spatial cells in a small region of a CFD computation. The goal is an ongoing estimation of the turbulence at spatial scales well below those that could possibly be resolved by a macroscopic 3D CFD model.

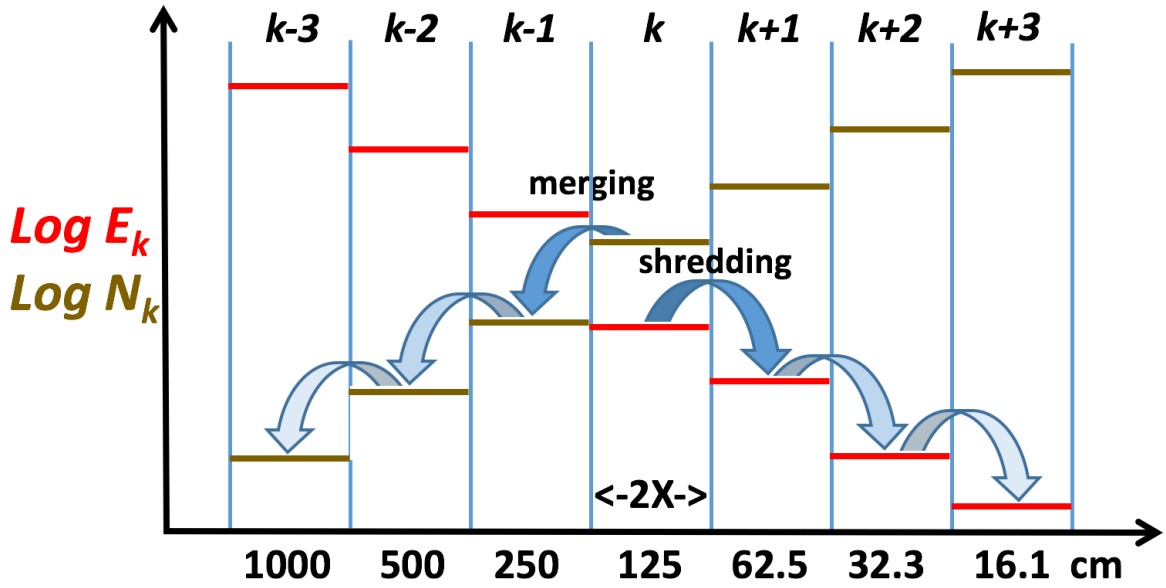

Figure 2.1. Schematic of the logarithmic k-space grid used in the Coherent Structure Dynamics model. The wavenumber increases and the corresponding turbulent scale size decreases to the right. The turbulent energy density (red) decreases from bin to bin with k, the bin index, while the rotor number density (brown) increases. The local effects of rotor merging and rotor shredding interactions is shown.

The vortex filaments, the coherent structures of turbulence, are divergence free and should close, at least at infinity. Here we will be concerned with idealized, localized coherent vortex structures which are being called rotors. The turbulent flow field is thought to be a superposition of rotors of many different scales and strengths that interact among themselves locally producing nonlinear turbulent behavior that is controlled, overall by the Navier-Stokes equation, and thus the fluid dynamics that we know. This is, I suppose, a kind of wavelet representation. Here the rotor scales are discretized into logarithmic bins, each a factor of two in scale different from the next longest and the next shortest wavelength as shown above. With 30 bins, a turbulent spectrum can span 9 orders of magnitude.

Rotors at a given scale can all have different strengths and orientations but it is dynamically interesting to simplify all rotors in a local volume as having a single kinetic energy at each scale. There clearly has to be some consideration given for nearby rotors having different energies but, for now, we consider this distribution to be a delta-function at the average energy density. The average energy varies as it enters and leaves a given bin during nonlinear fluid dynamic interactions. Another assumption we are making is that interactions between rotors of different scales occurs between adjacent bins only. Brasseur and colleagues have shown that most of the energy transfer in turbulent cascade occurs locally in k space.

Two nonlinear rotor interactions (processes) are considered:

Rotor Shredding/Forward Cascade generates new rotors (vortices) of size R_{k+1} from interactions of the rotors at the next larger size R_k. We can think of shredding as two rotors tearing at each other until their energy has all be transfers to rotor filaments of half the scale size. In principle, there can be may forms of shredding depending on rotor alignment and separation, etc. Here they are all lumped into one generic nonlinear interaction whose strength will be calibrated.

Rotor Merging/Inverse Cascade generates rotors of size R_{k-1} by merging two rotors of the next smaller size R_k. Inverse cascade is expected to be much weaker than forward cascade in nearly all situations.

The CSD representation, with grid sizes varying by a factor of two, facilitates a very simple treatment of the merging and shredding operations. The merging and shredding operations at each scale will be assumed to proceed at a rate equal to the precession time τ_k of two rotors about each other with average energy E_k and average separation S_k. This time depends on the average characteristic rotor velocity V_k and a non-dimensional packing fraction expressing how fully the volume is full of rotors at each scale k. Certainly the absolute strength of these interactions can be calibrated by DNS but that is not necessary at this stage because any multiplicative factor can be absorbed by rescaling the time. Further, a whole range of different interactions could be defined including non-local interactions connecting distant bins. However, these two interactions, merging and shredding, suffice. Further, for the two interactions identified, when distributions of rotor properties in each bin are admitted, much more detailed dynamics and varied rotor end states could be included in the model.

A third process, viscous rotor decay is also important, particularly at small scales. Rotor Decay reduces the kinetic energy E_k of rotors of size R_k diffusively due to viscosity without changing the number of rotors N_k or the packing fraction P^f_k. Thus viscous dissipation terminates the Kolmogorov cascade. The resultant heating is not tracked in this model.

The total turbulent kinetic energy per unit volume in the system is $E_{tot} = \sum_1^{kmax} E_k$. There may be external energy sources, for example at long wavelengths, but the total energy is generally conserved in the so-called "inertial range." This means that energy leaving one scale is exactly added to the next larger or next smaller scale in this model. These rates are proportional to τ_k, the rotor interaction time defined above.

The non-dimensional packing fraction mentioned above, P_k^f, is defined in Eq. 3.6 below to show how much of the volume actually has rotors of scale k in it. Rotors of all different scales may overlap but when the rotors of a particular scale are close together they must interact strongly and thus cannot overlap appreciably without either merging or shredding. If they are far apart they will interact at most weakly. When the packing fraction becomes small, the rotors are farther apart but they are also stronger because there are fewer of them to share the kinetic energy density E_k. As a result, the characteristic velocity of each rotor will be larger and the interaction times τ_k become smaller.

3. The Structure of a Rotor

Figure 3.1 shows the structure of a representative rotor of size R. Rotors are conceptualized as coherent vortex structures with a fixed vorticity strength ω which is constant inside radius R and zero outside. The azimuthal velocity associated with this rotor is

$$v_\phi(r) = \frac{rV}{R} \text{ inside } R \quad and \quad v_\phi(r) = \frac{VR}{r} \text{ outside } R. \qquad \text{Eq. 3.1}$$

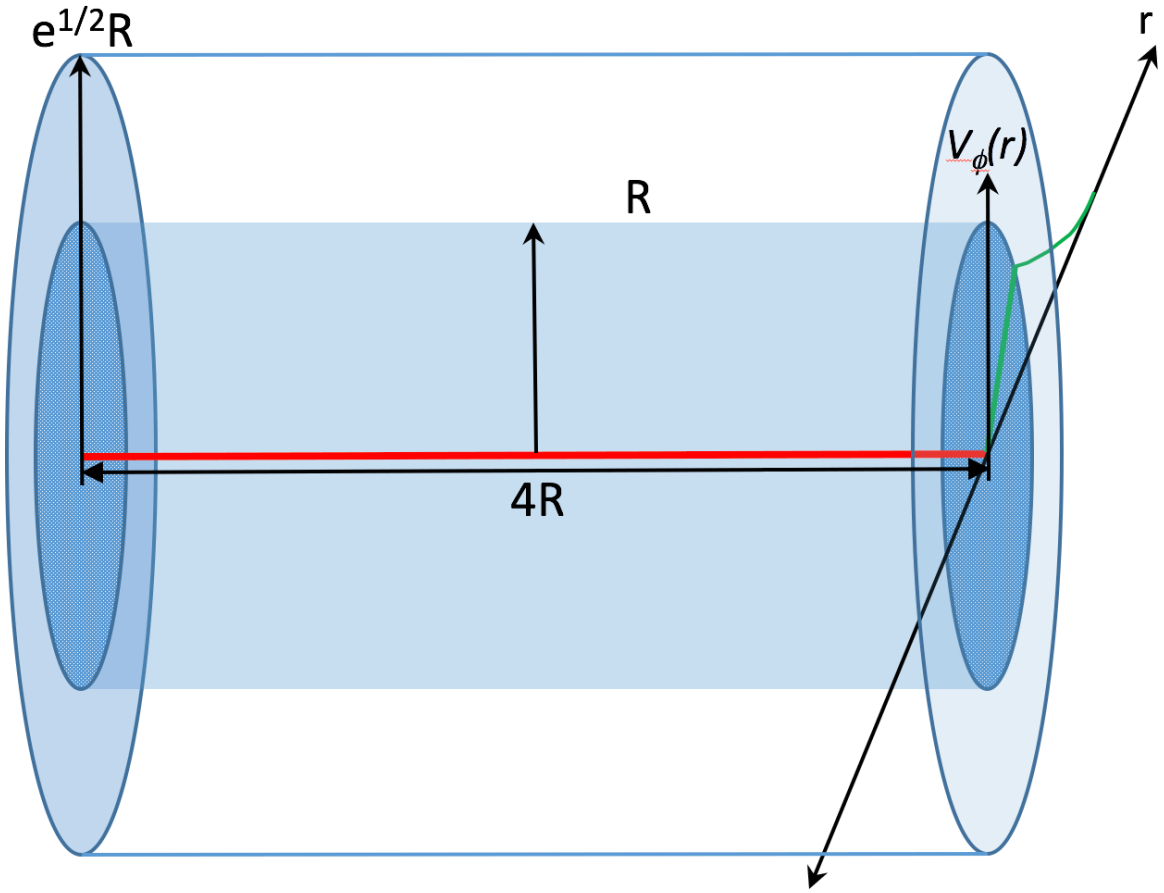

Figure 3.1. Structure of a rotor of size (scale) R. Vorticity is uniform inside R and zero outside. The corresponding azimuthal velocity profile is shown in green. The velocity field is cut off at radius $e^{1/2}R$ due to shielding from the composite "turbulent" flow field.

These rotors are ascribed a finite length in the axial (Z) direction. It is reasonable to choose this length to be $4R$ to define a relatively compact structure. There is nothing driving these choices other than common sense and a desire to keep the model computable. These choices have little computational import since the parameters scaling the strength of the rotor interactions can absorb different choices of these rotor parameters. As with wavelets, there is great freedom possible in choosing a complete basis, so these choices can be made for convenience and simplicity. As these rotors are localized vorticity structures, the vortex lines must form closed loops with no divergence. This necessary "cladding" of the bare rotor core is not shown in Fig. 3.1 but is assumed. The main consequence for this model is that the velocity field of each rotor drops off more quickly than indicated in Eq. 3.1 and thus distant interactions of rotors, when their separation is large, become smaller. This effect can be incorporated in the model and will be described below.

Because vorticity and turbulence are closely related, the simple properties of a rotor have to be constrained by momentum and energy conservation. Energy conservation is treated explicitly in the governing equations. Momentum conservation is treated implicitly in the sense that each rotor induces a velocity fleld that has no net momentum. As a result, the aggregate momentum associated with each bin is zero. Any net momentum is assumed contained in the macroscopic flow that drives the CSD model. The vorticity associated with $v_\phi(r)$ above is given by $\omega \equiv \frac{1}{r}\frac{d}{dr}\left(rv_\phi(r)\right) = 2\frac{V}{R}$. This is constant when $r < R$ and zero otherwise. Circulation is a concept often used: the integrated vorticity piercing an area or equivalently, the line integral of the velocity along the periphery of that area. For the rotor defined above, this line integral is

$$C = 2\pi RV. \qquad \text{Eq. 3.2}$$

C has units of cm^2/sec. Circulation, as a defined quantity, has limited use here since the velocity line integral around a volume of isotropic turbulence is expected to be about zero due to cancellation of fluctuation velocities associated with a whole distribution of rotors.

The kinetic energy of a single rotor is a volume integral over the square of the velocity multiplied by *4R*, the nominal extent of the rotor in the Z direction:

$$\varepsilon = 4R \int_0^\infty \frac{1}{2} \rho \, v_\phi^2(r) \, 2\pi r dr \qquad \text{Eq. 3.3}$$

Using Eq. 3.1 above, the integral in Eq. 3.3 is broken into two pieces to be integrated analytically.

$$\varepsilon = 2\rho R \int_0^R \left(\frac{rV}{R}\right)^2 2\pi r dr + 2\rho R \int_R^{R_\infty} \left(\frac{VR}{r}\right)^2 2\pi r dr$$

$$= \pi\rho R^3 V^2 + 4\pi\rho R^3 V^2 ln\left(\frac{R_\infty}{R}\right) \qquad \text{Eq. 3.4}$$

Most of the contribution to the kinetic energy of a rotor comes from the flow outside the vorticity-containing core. In Eq. 3.4, R_∞ is a radius larger than R_k beyond which the rotor fluid velocity at scale k is smaller than other contributions. Using a finite value of R_∞ is one manifestation in the model of the required divergence-free cladding of the rotor core mentioned above. This radius cutoff keeps the single rotor kinetic energy finite. When $R_\infty = \sqrt{e} \cong 1.649R$, for example, the average rotor kinetic energy at scale k is

$$\varepsilon_k \equiv E_k / N_k = 3\pi\rho R_k^3 V_k^2 \qquad \text{Eq. 3.5}$$

where N_k is the number of scale-k rotors per unit volume. This equation gives a way to calculate the characteristic rotor velocity at scale k from the primary variables E_k and N_k.

It is useful to define the packing fraction of these rotors as

$$P_k^f \equiv 3\pi R_k^3 \, N_k. \qquad \text{Eq. 3.6}$$

The packing fraction is a non-dimensional number that describes how isolated the coherent structures at each scale are from each other. A small packing fraction means that the rotors are far apart relative to the characteristic radius R_k. When the packing fraction is constant over all bins, scale similarity, in the sense usually meant, is possible. In terms of the this packing fraction and the bin kinetic energy, the characteristic velocity of a rotor at the edge of its core is

$$V_k \equiv \sqrt{E_k / (\rho P_k^f)}. \qquad \text{Eq. 3.7}$$

Equation 3.7 shows that the characteristic velocity of rotors of scale k becomes large when the number density is small, for a given energy density, i.e. when the packing fraction is small.

When R_k is very small (large k), N_k will usually be correspondingly large as long as the relative separation of the rotors, given by

$$S_k \equiv R_k / \left[P_k^f\right]^{1/3}, \qquad \text{Eq. 3.8}$$

is of order R_k. When the separation between rotors is comparable to their size, the packing fraction will be near 1. This is considered to be a very limiting condition as it means that all rotors are overlapping and should no longer be treated as separate as they will be in the latter stages of merging or shredding.

3.1. Rotor Number Density

The number of rotors per unit volume N_k, which appears in Eqs. 3.5 and 3.6 above, is unknown and will also have to be part of the solution. N_k is in no way conserved. This number density will be allowed to vary along with the distribution of rotor velocities and energies between the various wavelengths. This is a significant extension relative to most theories leading to the Kolmogorov spectrum. Allowing N_k the freedom to evolve means that different scales in the inertial range are not necessarily scale similar. The number of rotors N_k per unit volume is coupled to the total energy E_k in that bin. Any interaction that creates a new rotor must necessarily reapportion the conserved energy to ensure that the new rotor actually has some energy. This could be an issue since the new rotors might not necessarily be created at the current average rotor energy for that bin. Interactions between rotors that create new ones will create them at a particular energy determined by the energy available from the rotors of smaller or larger scale that are being destroyed or created.

If we postulate that each interaction that creates or destroys rotors does this in a scalable manner that depends only on the relative geometrical configuration and the rotor energies, it is possible to define rate equations for the process. Fortunately, the rate equations postulated for the rotor number density mirror the form required by the stiff equation integrator to be used. An approach coupled to the calculated changes in bin energy is presented in which, the overall energy conservation is enforced. We will assume that the average rotor energy at scale k is the same for all these rotors so this average energy can be computed including conservation.

This model currently considers only binary interactions describing two rotors merging to form a larger one and two rotors shredding to form a number M of smaller rotors. This number need not be integral since a range of fluid dynamics shedding behaviors would seem to be possible and should be the same nondimensionally for all bins due to scale independence of the interactions in the inertial range. M is non-dimensional input parameter of this model and can in principal also be calibrated from DNS. These changes in rotor number density will still conserve rotor energies between the adjacent bins in k-space.

The viscous damping interaction, which extracts energy from a given scale, while possibly reducing the number of rotors at that scale, will be treated separately. Viscous damping will also be cast in the form of conservation rate equations. However, energy is extracted and converted to heat by viscous damping so this appears in the equations as an overall energy sink. Many additional types of interactions could be considered. However, only Navier-Stokes-Equation solutions are likely to give accurate, or at least defensible, results for any of the possible postulated interactions, so the current approach is to keep things as simple as possible. There will be a few non-dimensional parameters for these interactions that must be the same from bin to bin. These can be treated as calibration parameters.

During rotor merging, two rotors of like sign precess around each other several times while their mutual shear flow gradually smears them into each other. The simplest assumption is that after some number of precessions we will say the original rotors of scale R_k are gone and a new one of twice the size, $2\ R_k = R_{k-1}$, replaces them. The number of new rotors is half the number of original rotors, though the new rotor is nominally twice as long as the originals so a factor of two may still be in question.

It is important to stress that the CSD model is postulated, not derived here. It is designed to exhibit important physical properties and constraints throughout the range of scales represented but is not derived in any direct way from the Navier-Stokes Equations. Therefore, it is ultimately dependent on calibration for its quantitative relevance, as other models "derived" from experiment.

4. The Coherent Structure Dynamics Rate Equations

A simple conservation equation for turbulent energy cascade into bin *k* from the next larger scale *k-1* (i.e. rotor shredding or forward cascade) is:

$$\frac{dE_k}{dt} = \gamma \frac{\mho_{k-1}}{S_{k-1}} E_{k-1} - \gamma \frac{\mho_k}{S_k} E_k \qquad \text{Eq. 4.1}$$

where $\mho_k \equiv V_k \left(P_k^f\right)^{1/3}$ is the characteristic rotor velocity at the average rotor separation distance. This is the velocity with which typical nearby rotors will precess around each other. γ is a number, which can be calibrated, expressing how fast rotor merging occurs in terms of the precession velocity and distance. In this paper γ is set to 3.0 as determined by comparison with detailed simulations of the Taylor-Green Vortex (TGV) problem in the literature. This sets a scale for the time variable.

The full energy density equation, accounting also for rotor merging (inverse cascade) and viscous damping is

$$\frac{dE_k}{dt} = \gamma \frac{\mho_{k-1}}{S_{k-1}} E_{k-1} - \gamma \frac{\mho_k}{S_k} E_k + \delta \frac{\mho_{k+1}}{S_{k+1}} E_{k+1} - \delta \frac{\mho_k}{S_k} E_k - \nu \frac{1}{R_k^2} E_k \qquad \text{Eq. 4.2}$$

This equation is a rate equation whose form is dictated by dimensional considerations as well as physical arguments. The coefficient δ, analogous to γ, expresses how fast inverse cascade occurs. δ Is given the value $0.2\,\gamma = 0.6$ in the examples following as we expect inverse cascade to be weaker than forward cascade. The scale factors γ and δ are constant across all rotor size bins as required by scale independence of the inviscid aspects of the fluid dynamics. Being constant also ensures rigorous energy conservation summed over all scales. What leaves one scale must enter the next smaller (or larger) scale, with the exception of viscous damping and energy cascade beyond the largest and smallest rotor sizes, these latter becoming "boundary" conditions for the model. Both δ and γ are possible candidates for future detailed calibration.

$\mho_k/S_k$, appearing in the first four terms of Eq. 4.2, has units of sec^{-1}, as demanded to match the time derivative on the left. The velocity and distance variables $\mho_k$ and S_k are V_k and R_k adjusted for the current rotor separation at scale *k*, and thus depend on the rotor packing fraction. The term R_k^{-2} in the viscous term relates the dissipation rate, which should not depend on the rotor separation, to the bin rotor scale.

The full Eq. 4.2 can be rewritten in terms of the basic CSD variables as:

$$\frac{dE_k}{dt} = \frac{dE_k^{ext}}{dt} + \gamma \frac{V_{k-1}}{R_{k-1}} \left(P_{k-1}^f\right)^{2/3} E_{k-1} + \delta \frac{V_{k+1}}{R_{k+1}} \left(P_{k+1}^f\right)^{2/3} E_{k+1} - (\gamma + \delta) \frac{V_k}{R_k} \left(P_k^f\right)^{2/3} E_k - \nu \frac{1}{R_k^2} E_k . \qquad \text{Eq. 4.3}$$

The first term on the right hand side of Eq. 4.3 is an external energy source/stirring term, which will typically be applied only at the longest wavelengths. The next two terms on the right side of Eq. 4.3 are production terms for larger rotors and smaller rotors respectively based in scale-*k* interactions. These are followed by a combined destruction term from rotor shredding and merging at scale *k*. Finally, on the right, is the viscous rotor dissipation term. These production and destruction terms can be evaluated given the principal quantities at any time but their sum, external to the numerical integration, will not necessarily coincide with the effective values actually applied by the stiff equation integrator CHEMEQ2.

In addition to the nonlinear energy cascade governed by Eq. 4.3 above, we also need an equation to advance the rotor number density. This version of CSD will use

$$\frac{dN_k}{dt} = \frac{dN_k^{ext}}{dt} + \frac{\eta^s}{2}\gamma\frac{V_{k-1}}{R_{k-1}}(P_{k-1}^f)^{2/3}N_{k-1} + \frac{1}{4}\delta\frac{V_{k+1}}{R_{k+1}}(P_{k+1}^f)^{2/3}N_{k+1}$$
$$-\gamma\frac{V_k}{R_k}(P_k^f)^{2/3}N_k - \delta\frac{V_k}{R_k}(P_k^f)^{2/3}N_k - \nu\frac{F_k^{vd}}{R_k^2}N_k. \qquad \text{Eq. 4.4}$$

The first term on the right is an external source of rotors which will be present if, for example, the external energy source is provided by stirring. This equation is also in the form that can be integrated using CHEMEQ2 although it is explicitly not conservative. The factor ½ in the second term on the right indicates that one rotor is formed from two during merger. The term $\eta^s/2$ in the third term on the right indicates that two rotors shred each other to form η^s rotors in the next smaller-scale bin. These η^s new rotors will share the energy cascading down from the next larger scale with the already existing rotors at the smaller scale. η^s must be at least 8 or the packing fraction will tend rapidly to zero at small scales. In the examples below the value $\eta^s = 14.4$ is used, ensuring enough rotors to make up for merging, particularly at small scales. Appreciably larger values cause an instability as the energy of the individual rotors must decreases to counteract the extra rotors.

The viscous term in Eq. 4.4 is included to allow the removal of rotors that have become dynamically insignificant in time due to viscous decay. The viscous decay factor F_k^{vd} for each scale has yet to be determined. Here 1.0E-9 is used for all bins, indicating essentially no reduction in rotor number due to viscous dissipation. Viscosity here causes only a loss of average energy.

Consistency of Eqs. 4.3 and 4.4 can be shown. The destruction of rotors due to shedding at scale *k* has a rate of energy transfer to the scale *k+1* equal to $\gamma\frac{V_k}{R_k}(P_k^f)^{2/3}E_k$ from Eq. 4.3. In a small interval of time Δt this corresponds to an energy transfer of $\gamma\Delta t\frac{V_k}{R_k}(P_k^f)^{2/3}E_k$. This, in turn, corresponds to a number of rotors being destroyed,

$$\Delta N_k = -\gamma\Delta t\frac{V_k}{R_k}(P_k^f)^{2/3}E_k/e_k = -\gamma\Delta t\frac{V_k}{R_k}(P_k^f)^{2/3}N_k, \qquad \text{Eq. 4.5}$$

as appears directly in Eq. 4.4. Here $e_k \equiv E_k/N_k = 3\pi\rho R_k^3 V_k^2$ is used from Eq. 3.5 above.

5. Solving the Energy and Number Density Equations

The CSD model is advanced in discrete, macroscopic time steps dt, which may contain many smaller steps as determined by the CHEMEQ2 algorithm. The changes in the set of rotor energy densities $\{E_k\}$, rotor number densities $\{N_k\}$, and their corresponding packing fractions $\{P_k^f\}$ are determined using the stiff equation integrator CHEMEQ2 because the shortest wavelength, largest *k*, bins are mathematically stiff and thus demand an impractically short explicit time step. This integration will be highly nonlinear so care must be taken to ensure that energy conservation is preserved acceptably well - with the exception of viscous damping at short wavelengths.

The set of rotor energy densities $\{E_k(t)\}$ will be known at the beginning and the end of the step from time t_m to t_{m+1} so the integrated energy density change during the time step due the numerical integration is easily calculated.

$$dE_k(t_{m+1/2}) = E_k(t_{m+1}) - E_k(t_m). \qquad \text{Eq. 5.1}$$

In order that the values of the independent variables and the derived quantities can be synchronized, both Eqs. 4.3 and 4.4 must be integrated together. Thus $2k_{max}$ equations are solved simultaneously.

Equation 4.3 appears to be linear in the energies, with coefficients suggested by scaling and scale similarity arguments, even though the rotor interactions are being considered to be binary. Nonlinearity enters through the V_k terms. Any two rotors can interact, creating smaller rotors and merging to create larger rotors. This suggests that the number of interactions each rotor undergoes should be proportional to the density of rotors. However, the total number of binary interactions at each size scales as N^2.

The apparent linear dependence shown reflects an additional consideration: the strength of these interactions varies greatly with distance. Nearby rotors interact much more strongly than widely separated rotors whose interactions will also statistically tend to cancel. This distance shielding effect means that there will be a finite number of the closest rotors whose interactions matter most. Here this number, call it *M,* is taken as constant independent of the average separation of the rotors, which is captured by the packing fraction P_k^f. *M* might be estimated from Monte Carlo sampling or even "measured" from detailed numerical simulations (DNS). *M* is subsumed in the coefficients γ and δ in Eqs. 4.3 and 4.4. Thus the number of meaningful rotor interactions per unit volume is expected to be linear in the number of rotors per unit volume even though the number of interactions at any one time might appear to be mathematically quadratic. The strength of the meaningful interactions increases when the packing fraction is larger and this correspondingly increases the shredding rate and merging rates. These dependences are taken into account in the equations above by the interaction velocity and distance, $\mho_k$ and S_k.

6. The Kolmogorov Energy Spectrum and Viscous Dissipation

The Kolmogorov energy spectrum for the steady-state cascade of turbulent kinetic energy from large scales to smaller scales can be derived from dimensional considerations, a very strong argument. It has been demonstrated and verified in a number of ways including direct numerical simulations (DNS) and experiments. One way to derive this in CSD is to consider detailed balance in equilibrium. This requires the time derivative in Eq. 4.3 to be zero: thus

$$\frac{V_{k-1}}{R_{k-1}}\left[P_{k-1}^f\right]^{2/3}E_{k-1} = \frac{V_k}{R_k}\left[P_k^f\right]^{2/3}E_k = constant. \qquad \text{Eq. 6.1}$$

This can be written as $V_k\left[P_k^f\right]^{2/3}E_k = constant\ R_k$. Using Eq. 3.7, this can also be written as

$V_k\left[P_k^f\right]^{2/3}E_k = E_k^{\frac{3}{2}}\left[P_k^f\right]^{2/3}/\sqrt{1/(\rho P_k^f)} = constant\ R_k$. which in turn yields

$$E_k^{3/2} = constant\sqrt{\rho P_k^f}\ R_k^{3/2}. \qquad \text{Eq. 6.2}$$

Since the rotor scale R_k as proportional to the inverse wavenumber k^{-1}, Eq. 6.2, is the usual Kolmogorov inertial range spectrum with $\varepsilon_k = \frac{E_k}{k} \sim k^{-5/3}$ when the packing fraction is constant. In simulations, as we will see, P_k^f decreases throughout the inertial range but very slightly compared to the orders of magnitude variations in the rotor velocities, number density, and energy density.

Every rotor decays by viscous dissipation. This is unimportant at long wavelengths, i.e. large R_k. However, when R_k is small enough, viscous decay becomes important and we have left the inertial range. Viscous decay becomes faster than the rotor turn-over time which has the characteristic rate V_k/R_k. In CSD, Eq. 4.3 has a term of the form ν/R_k^2 where the viscosity ν has units of cm^2/sec.

$$\frac{dE_k}{dt} = \gamma \frac{V_{k-1}}{S_{k-1}} E_{k-1} - \gamma \frac{V_k}{S_k} E_k - \nu \frac{1}{R_k^2} E_k \qquad \text{Eq. 6.3}$$

Equation 6.3 is still in canonical form for integration as a stiff rate equation but now has another term that can be stiff, viscous dissipation, when the scale approaches the Kolmogorov scale.

Rotors at a given scale can all have different strengths and orientations. Fossil turbulence (Woods,1969; Gibson,1999) is very weak compared to other active nearby structures (rotors) of the same scale that may be inhabiting the system. The energy at each scale is nominally shared among all of the rotors but the fossil rotors may be large in number and yet not contributing to the fluid dynamics substantially. This situation suggests considering a distribution of rotor energies – or at least considering two classes, those that are dynamically significant and those that are not. The available energy would only be shared among the dynamically significant rotors. These considerations can play into how we should treat the packing fraction.

7. Calibrating CSD Using the Taylor-Green Vortex Problem

The two independent parameters for shredding and merging, γ and δ, apply to all scales but their values do not come from theoretical analysis. A program of detailed numerical simulation could provide answers, in principle, but first 'shredding' and 'merging' would have to be defined in an analyzable scale-independent manner. An approximate calibration can be provided using work already performed by researchers who have published detailed CFD solutions the Taylor-Green Vortex (TGV) problem (Drikakis, et al., 2007; Adams, et al., 2007; DeBonis, 2013; Kajzer, et al.,2014; Diosady and Murman, 2015; G. Giangaspero, et al., 2015; Grinstein, et al., 2018). The TGV problem is a triply periodic fluid-dynamic problem with a precisely defined, smooth initial condition that transitions to turbulence. In the detailed numerical simulations, the total energy in the system dissipates due to a combination of viscous and numerical dissipation at and near the spatial grid scale. The overall system dissipation rate is small for a time as the largest scale TG vortices interact but the rapidly peaks as shorter scales with faster interaction rates are energized. The total system energy then decays as a combination of cascade below the CFD grid scale physical viscous dissipation, if included, and any numerical dissipation present to provide stability and/or monotonicity.

The TGV problem can also be applied a good test of CSD energy conservation. During the first few seconds, before the forward cascade of energy reaches beyond the inertial range, the total energy is being reapportioned between the inviscid rotor scales but viscous dissipation, or cascade off the small-scale end of the grid, has yet to occur. When the viscosity is finite, some small dissipation of even the largest scales occurs but this can be made quite small when ν is small. Unlike CFD, the CSD model does not need numerical diffusion for stability. Taking the initial vortex (rotor) size and velocity to be 324 cm and 100 cm/sec respectively, and using the viscosity of water, $\nu = 0.01$ cm^2/sec, gives a baseline Reynolds number of

$$R_e = \frac{V_2 R_2}{\nu} \approx 3x10^6. \qquad \text{Eq. 7.1}$$

The dissipation rate for the CSD system is the rate of change of the total turbulent kinetic energy. When the nonlinear cascade reaches the dissipation zone where the spectrum begins to fall off quickly, the viscous dissipation increases rapidly, peaks, and then begins to drop as the total energy in the system is being drained away at the short wavelength end of the spectrum. Since the inviscid cascade continues feeding the dwindling kinetic energy down to the viscous zone even after the dissipation peaks, the time that the dissipation peak is reached and the rate of decrease of the global dissipation after the peak are good measures of the choice of the parameters γ and δ.

The CSD model, programmed in Fortran 90, is currently being run on an iMac with a four 3.5 gigahertz cores. The numerical solution is advanced using CHEMEQ2 (Mott and Oran, 1991 and references therein) to integrate the stiff dynamic rate equations. The performance and convergence is considered further in Section 8. There are several parameters in the model that affect the performance and testing has been, by no means, completed although several scenarios including a number of parameter variations have been performed. Several of the obvious calibrations and tests are described in this section and the next.

A short series of CSD computations was performed varying γ and δ to match the curves in Figs. 4a.4 and 4a.5 of Drikakis, et al., 2007. The initial conditions for CSD were taken as V_2 = 100 cm/sec with a system size of 628 cm (~ 100 x 2π). These choices, with a packing fraction of 0.9 initially, allows the appropriate non-dimensional time t^* to be measured in seconds. Initializing energy only in bin 2 corresponds approximately to the 8 counter-rotating vortices of the Taylor-Green problem. A number of runs showed that $\gamma = 3.0$ and $\delta = 0.6$ give reasonably close agreement with the late time dissipation rate – making the time scale for CSD evolution agree closely with the fluid dynamic simulations.

The smooth initial conditions of the Taylor-Green problem undergo a period of laminar instability before nonlinear cascade can truly be said to begin. This growth period is not included in the CSD model but the effect can be approximated by an initial delay followed by a ramp up of the coefficients γ and δ to their calibrated values. A "linear growth" delay of 3 seconds followed by an 8 second linear ramp-up of γ and δ places the dissipation peak at about 9 seconds as seen in the table below, in close agreement to the CFD results. This calibration is at least semi-quantitative, let's say at the 10% level, but not too much should be made of the quality of agreement with the detailed simulations, which even differ appreciably among themselves. As an added note, other problems may need to be initialized in different ways for different driving terms or boundary conditions.

Table 7.1 Dissipation Rates at Selected Times

dt = 1.0 second		dt = 0.5 second		dt = 0.25 second		dt = 0.1 second	
time	dEtot/dt	time	dEtot/dt	time	dEtot/dt	time	dEtot/dt
9.0 s	844.995	8.50 s	901.225	8.75 s	957.067	8.80 s	966.895
10.0 s	849.651	9.00 s	936.937	9.00 s	963.453	8.90 s	969.748
11.0 s	766.365	9.50 s	932.932	9.25 s	959.642	9.00 s	969.571
20.0 s	158.079	20.0 s	157.851	20.0 s	158.306	20.0 s	157.200
30.0 s	60.362	30.0 s	59.373	30.0 s	58.667	30.0 s	58.656
40.0 s	29.753	40.0 s	29.307	40.0 s	29.194	40.0 s	29.153

Table 7.1 above presents dissipation rates from four CSD runs of the TGV problem performed with $\gamma = 3.0$ and $\delta = 0.6$ and 30 bins performed with four different timesteps. The dissipation rates here are simply the time rate of change of the total integrated system energy. No attempt has ben made to normalize these rates to any of the detailed simulations. The nominal Reynolds

number for all four cases in Table 7.1 is ~$3x10^6$. The timestep used appears above the two-column table of data associated with each of the four runs. The three shaded rows display the dissipation rates for the three timesteps straddling the peak dissipation, which occurs at slightly different times in each case. The shortest timestep run, the last two columns in the table, shows the highest peak dissipation and the most rapid kinetic energy drop off thereafter. The decay phase is illustrated for each case, i.e. each different CSD integration timestep, by the global dissipation results at 20 seconds, 30 seconds, and 40 seconds. Remember, these times in seconds are also numerically equivalent to the non-dimensional time due to the choice of initial conditions.

Figure 7.1 below shows the time evolution for four CSD runs, each at the shortest 0.1 second timestep, with different values of viscosity ν spanning a range of one million. The values used were ν = 100 (Re ~ 300), ν = 1.0 (Re ~ 30,000), ν = .01 (Re ~ 3 million), and $\nu = 10^{-4}$ (Re ~ 300 million). The two highest Reynolds number curves in the figure, red and lavender, are virtually identical because they are essentially inviscid. Even the *Re ~ 30,000* run, displayed as the blue markers every fifth timestep, gives essentially the same result. There is no indication of the peak becoming progressively sharper, however, as seems to occur in Figs. 4a.4 and 4a.5 of Drikakis, et al. Regardless of where the dissipation zone, is the global dissipation rate is controlled by how fast the kinetic energy cascades through the inertial range.

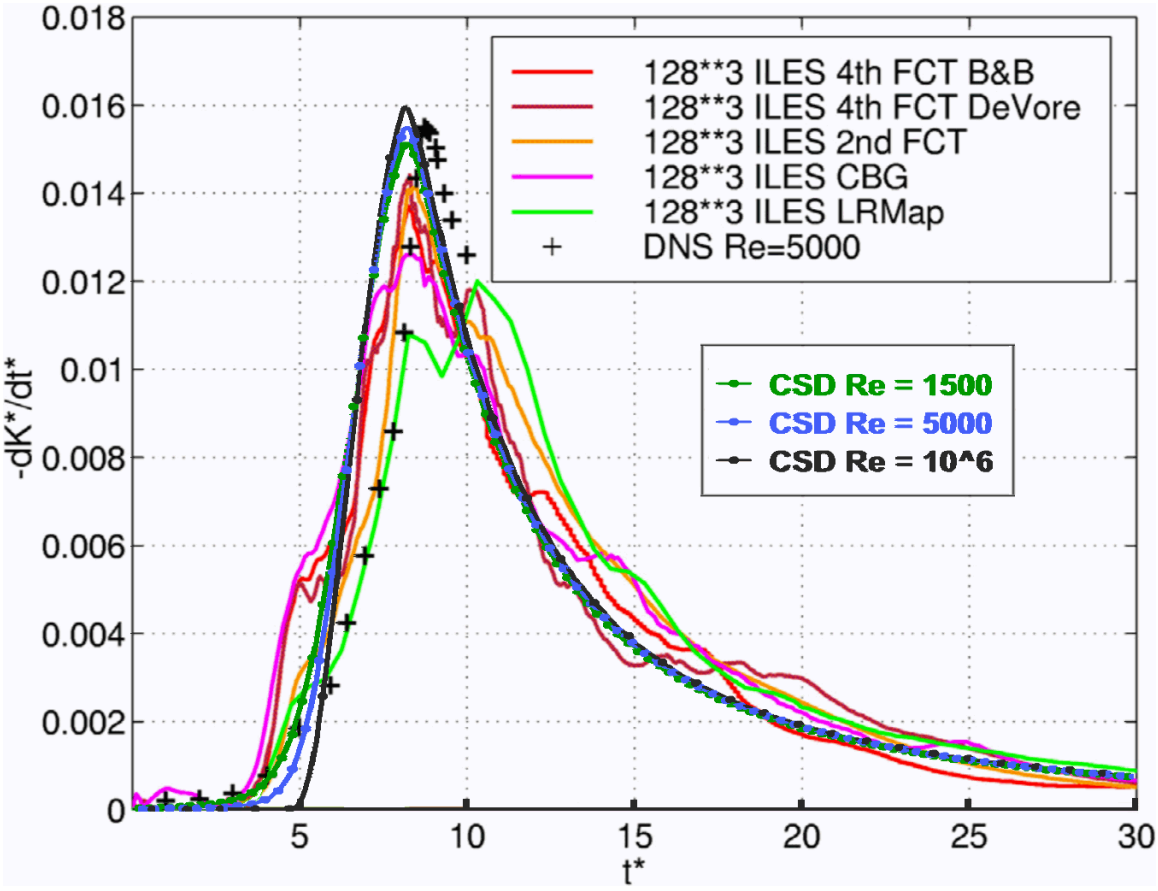

Figure 7.1. Dissipation rate of the turbulent kinetic energy for the Taylor-Green transition to turbulence problem. Three CSD solutions for different Reynolds numbers are compared to ILES and DNS solutions presented by Grinstein, et al. This comparison was used to set the free γ parameter in CSD. For Re ~ 1500 (green) and smaller, viscous dissipation begins immediately and lowers the peak dissipation rate.

7.1 Energy Conservation in Coherent Structure Dynamics

The discussion of energy conservation in CSD should be continued. The CHEMEQ2 integrator does not necessarily conserve the summed dependent variables exactly even when the underlying equations are in explicit conservation form. The current formulation (Mott and Oran) uses a predictor-corrector formulation but the algorithm is asymptotic when it detects mathematically stiff terms. These asymptotic formulae deal with the near cancellation of the mathematically stiff terms quite accurately but they do not necessarily conserve. This is a price paid for time steps appreciably longer than the stability limit.

Conservation can be guaranteed, in principle, by a fully implicit formulation but the numerical precision may have to be very high and the computational cost is extreme when the number of equations is large. CSD has about 50 nonlinear equations to be solved for a ratio of scales from longest to smallest of abut 10^8. The fully implicit approach requires multiple 50x50 matrix inversions within each iteration at each time step. The numerical community has expended a lot of effort to reduce the cost of such implicit computations but the expense is still very large. Further, in the end analysis, the accuracy is not high. The implicit approximation is stable but the characteristic time scales are greatly in error when the time step is larger than the explicit stability limit (Oran and Boris, 2001, Chapter 4). An asymptotic approach such as CHEMEQ2 limits the production and destruction evaluations to just the nonzero elements and does not do this a large number of times. The asymptotic formulae are actually more accurate, excepting the problem with exact energy conservation. In any case, external energy source terms at large scale and viscous damping at small scale are non-conservative terms that will effectively mask all but very large errors.

Since conservation cannot be strictly enforced, it must be checked. The total energy at the beginning and end of the step can be evaluated using $\mathcal{E}(t_m) \equiv \sum_{k=1}^{kmax} E_k(t_m)$. Without external sources adding energy, the difference, $\mathcal{E}(t_{m+1}) - \mathcal{E}(t_m)$, should be attributable to viscous damping added up over all bins. The total kinetic energy going from one step to the next step should be conserved when taking proper account of the source and the dissipation terms, both of which should ensure that the bin energies affected stay positive. Conservation is seen for the high Reynolds-number cases in Fig. 7.1 as evidenced by the zero dissipation values out to about 6 seconds on the left-hand side of the plot.

$$\mathcal{E}(t_{m+1}) = \mathcal{E}(t_m) + dt \sum_{k=0}^{kmax} \frac{dE_k^{ext}}{dt}\left(t_{m+1/2}\right) - dt \sum_{k=0}^{kmax} \frac{dE_k^{visc}}{dt}\left(t_{m+1/2}\right) \qquad \text{Eq. 7.2}$$

Ensuring positivity of the individual bin energies is a possible problem when any of the terms in Eq. 7.2 have the wrong sign. Negative external sources would be unusual but, if present, should not scavenge energy that is not there. The viscous terms are negative and they are large at short wavelength. Fortunately, CHEMEQ2 will prevent negative values with even the fastest damping terms although conservation may suffer. In the viscous case, however, the bin energies at high wavenumber are small so the non-conservation errors that occur will also be small.

Further numerical checks on non-conservation could be constructed but involve estimating the source terms and viscous damping terms exterior to the integrator. These estimates will not be exactly equivalent to what the integrator does except possibly for explicit sources at large scale. In any case, these estimates will be unable to cast much light on non-conservation caused by the stiff nonlinear cascade terms coupling the differing-scale bins. The simpler approach to study non-conservation is to do it empirically by running additional test cases. The Taylor-Green problem used to calibrate the primary parameters of the model is also a good test case for checking conservation in the nonlinear "cascade" terms governing shredding and merging of rotors. As can

be seen in Fig. 7.1, the essentially identical global dissipation values of the three high Reynolds-number cases as a function of time is some evidence that non-conservation of energy in the integration has been controlled.

A second case, similar to the TGV problem was initialized with no energy in the longest wavelengths, i.e. smallest k, nor in the shortest wavelengths k near k_{max}, and with zero external sources. Moving the bin with initial energy to bin 6 allows a glimpse of the effects of inverse cascade. Again, for some number of time steps the initialized energy will remain in the inertial range where viscous damping may also be neglected. For this test, a velocity of 5 cm/s was initialized in bin 6 with rotors of size 31.25 cm. Values of with $\gamma = 1.0$ and $\delta = 0.2$ were used for this run to spread out the time scale. This corresponds to an initial total system energy density of 10.0 gm-cm/sec^2 (Eqs. 3.5 – 3.7), all in one rotor-size bin. Table 7.2 is a map of how the conserved energy cascades up and down the spectrum from the initial delta function (red block at t = 0 s) in bin 6. Red indicates a rotor energy density greater than 1.0. Orange indicates bin energies between 0.1 and 1.0. Yellow indicates bin energies between 0.01 and 0.1. Green indicates bin energies between 10^{-3} and 0.01. Light blue indicates bin energies between 10^{-4} and 10^{-3}. Even lighter blue indicates bin energies in the range between 10^{-5} and 10^{-4} and clear indicates a bin energy less than 10^{-5}. The letter s is entered in each bin where the characteristic precession time, characterizing the interaction rate between rotors, is shorter than the 1-second timestep, i.e. where the equations are stiff.

Table 7.2. Energy Conservation Map: No Viscosity or External Driving Terms

time	Sum E_k	1	2	3	4	5	6	7	8	9	10	11	12	13	14	15	16	17	18	19	20	21	22	23	24	25	26	27	28	29	30
0 s	10.0000																														
1 s	10.0000																														
2 s	10.0000																														
3 s	10.0000																														
4 s	10.0000																														
5 s	10.0000																														
6 s	10.0001																														
7 s	10.0001																														
8 s	10.0001																														
9 s	10.0001																														
10 s	10.0001																														
11 s	10.0001																														
12 s	10.0001																														
13 s	10.0001																														
14 s	10.0001																														
15 s	10.0001																														
16 s	10.0001																										s	s	s	s	s
17 s	9.99657																			s	s	s	s	s	s	s	s	s	s	s	s
18.s	9.97274																		s	s	s	s	s	s	s	s	s	s	s	s	s
19 s	9.92240																	s	s	s	s	s	s	s	s	s	s	s	s	s	s
20 s	9.83360																	s	s	s	s	s	s	s	s	s	s	s	s	s	s

Table 7.2. Map of the initial spread of a local energy spike at bin 6 throughout the turbulent distribution. Viscosity and driving terms are switched off to highlight energy conservation/non-conservation. Red = bins with $E_k > 1.0$. Orange = E_k between 0.1 and 1.0. Yellow = E_k between 0.01 and 0.1. Green = E_k between 10^{-3} and 10^{-2}. Blue = E_k between 10^{-4} and 10^{-3}. Pale blue = E_k between 10^{-5} and 10^{-4}. Clear = $E_k < 10^{-5}$. "s" indicates mathematically stiff bins.

By 20 seconds elapsed time, when significant energy first begins to cascade off the short-wavelength end of grid, the three bins 6, 7, and 8 still contain nearly 70% of the system energy. As can be seen in Table 7.3, essentially none of the energy has reached to longest-wavelength bin due to inverse cascade, which is relatively weak. E_1 is still 4.0E-13 and E_2 has increased only to

4.95E-12. The increase in total energy by one part in 10^5, evident first between 5 and 6 seconds in the table above before the energy spread has reach either boundary of the scale-space grid, can be attributed to the finite error tolerance for convergence of the predictor-corrector algorithm in CHEMEQ2. Until 15 seconds, energy has not even begun to reach the short-wavelength end of the spectrum. CSD allows energy cascade smoothly off of the spectral grid, even in the absence of viscosity. The power law spectra are followed closely up through the last bin without any dissipation zone so the solutions are not exactly the same as in the previous figures. The point is, however, that the equation set and the numerical solution are well behaved.

Once energy conservation of the solution procedure has been established, a second test involves measuring the effects of viscous dissipation. This effect, summed over all bins using Eq. 7.1, will become dominant eventually with or without external source or driving terms. When viscosity is turned back on, with a value of 0.01 cm^2/sec, approximately the viscosity of water at 72 ^{0}F, much greater energy non-conservation in the grid is seen. The following values of the total energy per centimeter^3 are observed at 0, 2, 4, 6, 8, 10, 12, and 14 seconds into the run: 10.0000, 9.99974, 9.99936, 9.99878, 9.99784, 9.99619, 9.99280, and 9.98376 erg/cc. Energy conservation is still observed to 2 parts per 1000 at the end of the 14 seconds but energy loss from the system is increasing rapidly. As the short-wavelength end of the spectrum becomes excited, where viscous dissipation is strongest, energy conservation on the grid decreases quickly. In the next six seconds, the energy cascade reaches to and through the dissipation zone.

At 15 through 20 seconds the summed energy densities, with viscosity active, are: 9.97299, 9.95269, 9.91708, 9.86154, 9.78268, and 9.68476 erg/cc. 3.02% of the energy is lost after 20 seconds due to viscosity and cascade, as opposed to 1.7% due to nonlinear cascade alone. This viscous energy is being lost from the bins that are on the grid with the effect of reducing the on-grid values and thus reducing the energy available to forward cascade off the spectral grid.

8. Non-Equilibrium Turbulent Evolution Using the CSD Model

Coherent Structure Dynamics was developed to afford a view into the time evolution of turbulence without the need for expensive time-dependent CFD simulations. The spectrum is computed directly without the need to post process individual 3D flow fields. Further, the CSD model is designed so the development of the spectrum of an ensemble of turbulent flow realizations could be approximated with one fast computation. Necessarily some detail will not be available. This section provides computations of the evolution of a completely non-equilibrium turbulent scenario in which an initially quiescent fluid is stirred continuously at the system size holding the energy density at this largest scale constant.

8.1. An Equilibrating Non-Equilibrium Turbulence Spectrum

For this problem, the model treats a single spatially homogeneous domain with only the 10-meter rotor size externally energized with a fixed characteristic rotor velocity of 2.0 m/s. This is the largest scale (bin 1) in the system. The variables, with the exception of the rotor number density and the packing fraction, are scaled by their values in the first bin, which are held fixed in this problem. Figure 8.1 below depicts this initial condition, which is as far from an equilibrium, Kolmogorov-like spectrum as possible. Essentially all of the energy is in the longest wavelength.

The equations are being solved with 0.1-second timesteps for this problem on a grid of 26 bins whose smallest scale is about $3x10^{-5}$ cm. The tests reported in Table 7.1 indicated that 0.25 and 0.1 second integrations were almost identical. For this problem, the equations for all rotors with sizes less than 1 or 2 cm, that is, bins 11 through 26, are mathematically stiff once the turbulent cascade is established.

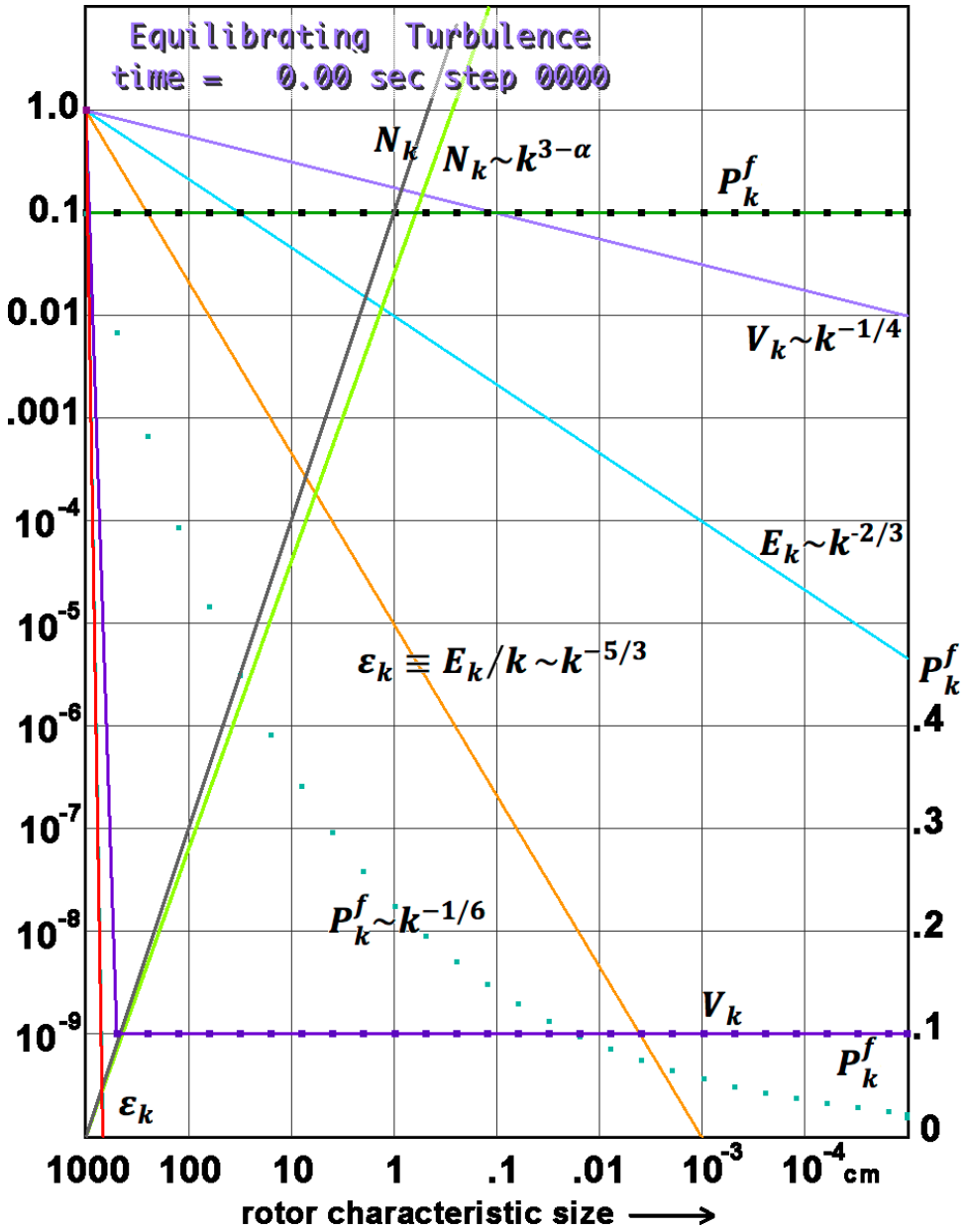

Figure 8.1. Initial condition for a CSD run demonstrating the transient equilibration of a highly non-equilibrium spectrum to a Kolmogorov-like steady state. The rotor velocity (lavender), energy density (cyan/light blue), spectral energy density (orange/red) and rotor number density (grey/light green) are shown on logarithmic scales.

Most curves in the figures to follow are normalized to 1.0 on the logarithmic y-axis. The logarithmic x-axis ranges from 1000 cm, the largest scale, down past 10^{-4} cm, which, for this problem, is below the dissipation scale. The ideal, theoretical, power-law curves are shown as straight lines on this plot. Lavender is used for the rotor velocity, initialized to 2.0 m/s in bin 1 and maintained constant for this case. The ideal, steady solution scales as $V_k \sim k^{-1/4}$. The actual rotor velocity values at t = 0.0 sec are shown as lavender squares on the lavender curve. With the exception of bin 1 these values are all initially below 10^{-7} of the driving 2 m/s value. The velocities in bins 2 through 26 evolve according to the equation set as the system is constantly being "stirred" in bin 1 at 2 m/s. Light blue is used for the power law rotor energy density, which scales asymptotically as $E_k \sim k^{-2/3}$. The numerical values of E_k are plotted in a darker color, cyan in subsequent figures, with black squares at the computed bin values to show up better. E_k does not

appear in the initial condition because all bin values other than the first, normalized to 1.0 are below 10^{-10} at the bottom of the plot.

The rotor energy density E_k is not the usual spectral energy density, which is defined to be $\varepsilon_k \equiv E_k/k \sim k^{-5/3}$. The extra factor of k is required because the bin size is proportional to k. ε_k ideally satisfies the -5/3 law, which is drawn in orange and is also normalized to 1.0 at the left. The rotor number density $N_k \sim k^{3-\alpha}$ is draw in grey. It increases rapidly to the right with decreasing rotor size. It is normalized to 10^{-10} on the y-axis so the curve will appear on the same plot as the other variables. When the packing faction is constant, N_k must scale as R_k^{-3} because halving the rotor size allows eight times as many rotors to fit in the same volume while maintaining the same relative separation. The approximate asymptotic rotor number density is plotted in light green and scales as $\sim k^{3-\alpha}$. The actual time-dependent packing fraction is plotted in darker green with black squares at the bin data points. In the initial condition of Fig. 7.1 the packing fraction is everywhere 0.9 and plotted on a linear scale whose y-axis values are shown at the right side of each plot. The packing fraction evolves in time and is observed empirically (computationally) to approach $P_k^f \sim k^{-1/6}$ in time, an approximate power law, which is shown by the cyan squares in the lower part of each figure.

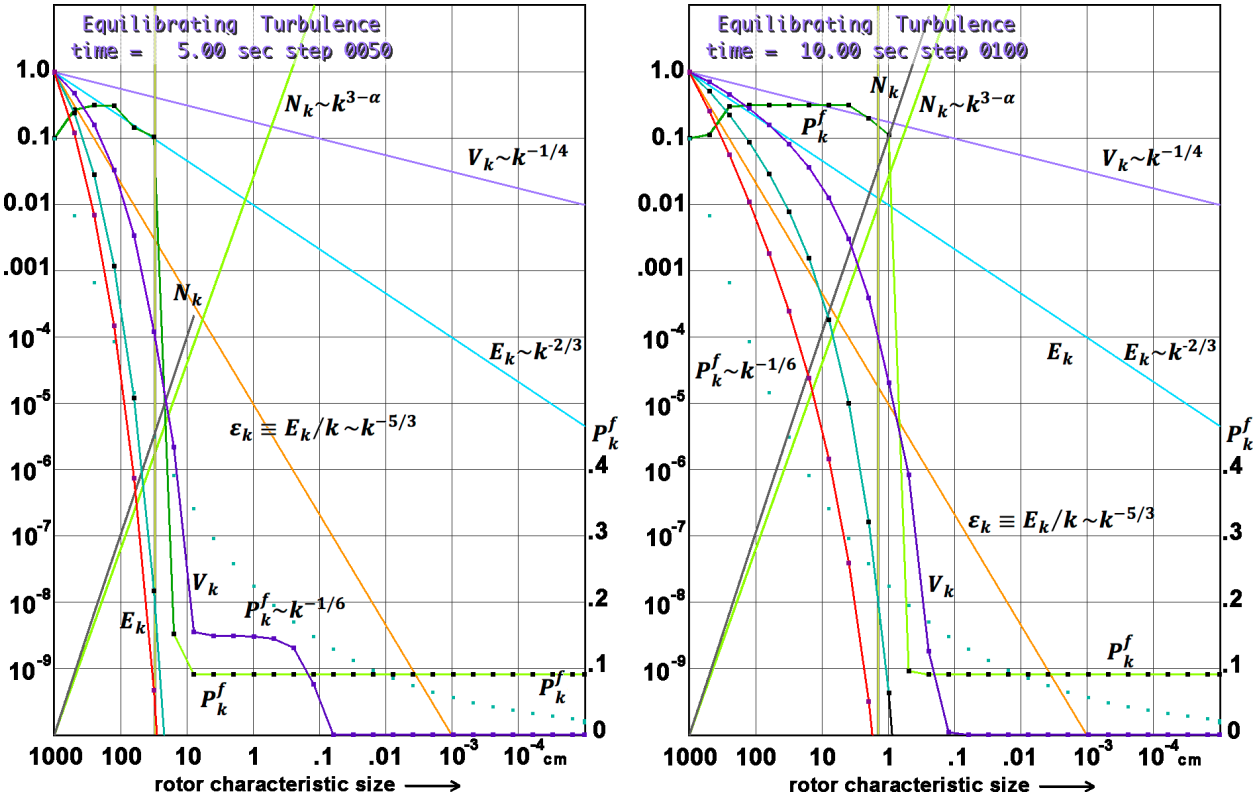

Figure 8.2. Left: After 5 seconds the cascade has spread down to the 10-cm scale and velocities have reached the 1-mm scale. Right: After 10 seconds the energy cascade has moved to 1-mm scales and a transient dissipation scale seems to have formed.

Figure 8.2 shows the variables of the CSD model at 5 seconds (on the left) and 10 seconds (on the right) after starting the run. At these early times the solution is effectively zero below a scale that decreases rapidly from 1000 cm at time zero. The packing fraction drops immediately to a value less than 0.1 in the small turbulence scales that have not yet been excited. At 5 seconds elapsed time, a foot of small but increasing rotor velocities has advanced down to the 0.1 cm scale and the velocity values at longer wavelength are increasing. By 10 seconds, the right-hand panel

in Fig. 7.2, a fledgling dissipation region has formed near 0.1 cm and advances to the right as the total energy in the spectrum continues to increase from the steady driving term.

Figure 8.3 shows the primary model variables at 20 seconds (left) and 30 seconds (right). The velocity and energy density profiles are beginning to approach the classical Kolmogorov spectrum dependence but the profiles still lie below the power-law curves. A vertical bar (yellow bordered by black) is drawn by the plotting program at the beginning of the dissipation zone where the viscous damping rate first exceeds the rotor-interaction rate. By 20 seconds the dissipation range for this problem is well established. By 30 seconds the maximum in the packing fraction, near bin 3 at 20 seconds, has moved to bin 1 leaving a monotonically decreasing profile into the dissipation zone. The grey rotor number density curve is also approaching its nominal, light green power-law curve. A pre-dissipation bump (also called the bottleneck) is beginning to form.

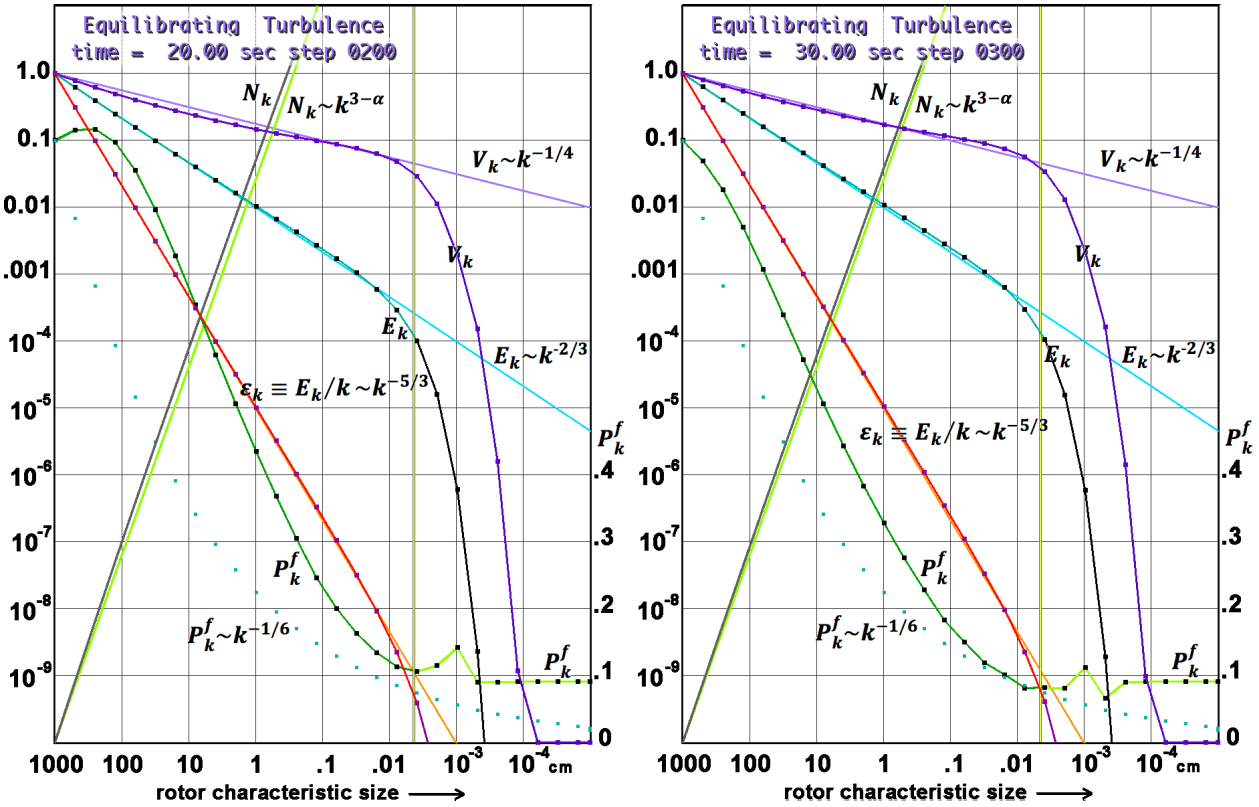

Figure 8.3. Left: After 20 seconds the spectrum is beginning to approach an equilibrium Kolmogorov spectrum with enough energy at short wavelengths to have established a dissipation scale. After 30 seconds the velocity and energy spectra are approaching power-law profiles throughout the inertial range although the pre-dissipative bump has not yet formed.

Figure 8.4 shows the equilibrating spectrum at 60 seconds after the run began. A well developed dissipation range begins at the vertical bar near 0.01 cm and extends for several bins to the right where the bin energy density E_k (cyan to black in the dissipation zone), spectral energy density ε_k (red to purple), and rotor characteristic velocity V_k drop off the bottom of the plot scale. Although the predissipative bump appears, Fig. 7.4 is still not fully equilibrated. The packing fraction, which is a non-dimensional variable, is not driven by the same dimensional arguments that constrain the spectral energy density and velocity and takes much more time than the velocity and energy density to relax to equilibrium. In fact, it takes another four minutes, until 300 seconds, for the computed spectrum to approach the "equilibrium" shown in Fig. 7.5. most notably, the packing fraction has now approached the power law approximation, which is plotting on a linear

scale by light green squares in the figures. The packing fraction is hard to define beyond the dissipation region and has been pegged at a fixed value of 0.09, a factor of 10 below the initial value. The pre-dissipative bump is well formed by 300 seconds and arises here because the viscosity reduces the energy in the short wavelengths to the extent that they become relatively ineffective at shredding the rotor energy into smaller scales so the energy can pile up.

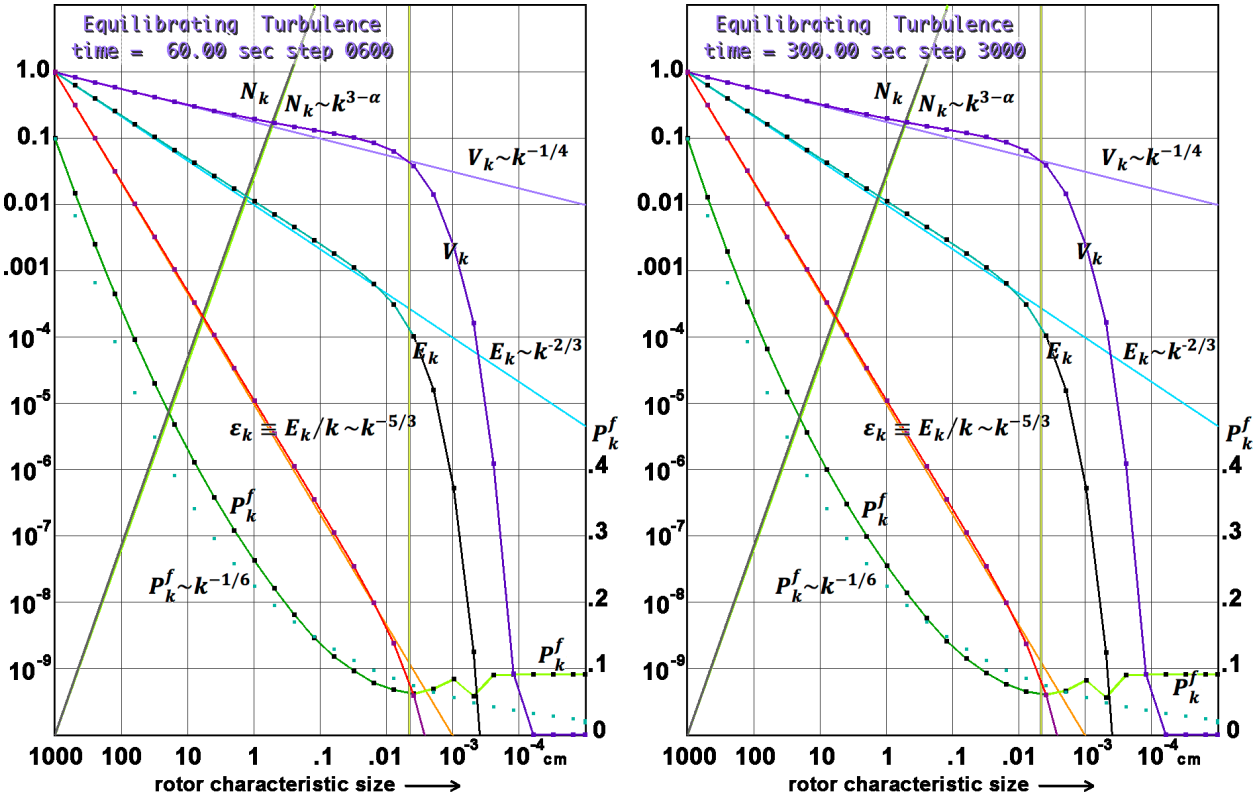

Figure 8.4. Left: After 60 seconds the transient turbulence spectrum calculated by the CSD model is approaching a Kolmogorov spectrum extending well into the dissipation scale at about 0.01 cm. The wavenumber increases and the corresponding turbulent scale size decreases to the right. The turbulent spectral energy density ε_k (red & blue) decreases from bin to bin with k, the bin index, while the rotor number density N_k (grey) increases. The packing fraction P^f_k (green) and the average rotor velocity V_k (violet) are also shown. Right: The fully equilibrated Kolmogorov-like spectrum at 300 seconds. The dissipation scale, where viscous damping of rotors exceeds their generation rate, is marked in both panels by the vertical yellow bar near 0.01 cm.

When viewed as a movie, the equilibrated spectrum on the right of Fig. 8.4 is seen to fluctuate in and beyond the dissipation zone by a couple of percent. This is the action of the integrator, working with a finite error tolerance, to treat the extremely stiff equations near the right edge of each of the plots. At the 10^{-4} cm scale, the equation characteristic time scales at 10^6 to 10^7 times shorter than the timestep.

8.2 Using Coherent Structure Dynamics in a CFD Code

The CSD model was designed to be fast enough to be run for many contiguous cells in one or more regions of a CFD computation without significantly impacting the execution of the CFD. Alternatively, a macroscopic CFD region could be pre-computed and stored for later processing with multiple dynamic realizations of highly resolved subgrid turbulence provided by Coherent Structure Dynamics for the same macroscopic CFD solution. In Subsection 8.3 below, the

performance and speed of CHEMEQ2 in executing CSD is discussed. Figure 8.5 shows one frame of a run with 64 separate non-equilibrium turbulent spectra being computed at once. Each separate computation is intended for a particular macroscopic CFD cell and was driven by a differently phased fluctuating rotor velocity in bin 1. These mimic a turbulent wake sweeping back and forth across the CFD cells of interest. The range of these excursions is shown by the width of the energy and velocity bands at the left edge of the figure. The characteristic rotor velocity in bin 1 varies by over one order of magnitude and the energy varies by over two orders of magnitude.

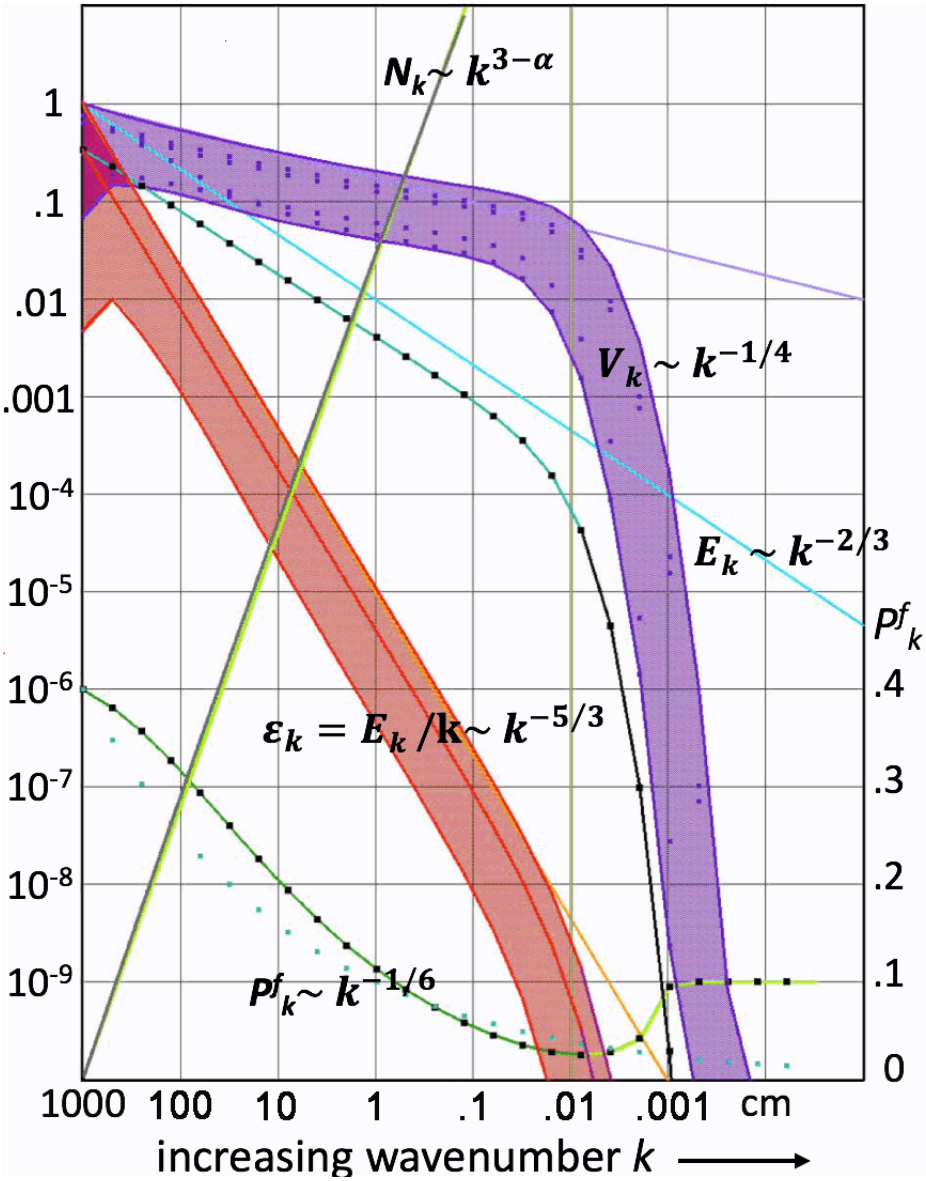

Figure 8.5. CSD run solving 64 separate turbulence evolutions simultaneously using a correlated random driver in each cell.

The bands in the figure display the range of velocity and spectral energy values taken on by the 64 separately evolving spectra over the entire scale range of ten orders of magnitude. Only one of the 64 packing fractions P_k^f and energy densities E_k are displayed to reduce clutter. To complete this application, the driving terms for each CSD spectrum would be coupled to a different CFD cell. Further, a model to lay down a consistent subgrid flow realization would be needed so a realistic higher-resolution flow field could be laid down in a spatially localized area such as a complex boundary layer or a region around a small UAV flying through the large-scale CFD flow computer.

8.3 The Execution Speed and Performance of CSD

The version of CHEMEQ2 used in the CSD program was programmed by Dr. Brian Taylor from the routines in Mott and Oran (2001). CHEMEQ2 contains a significant generalization and upgrade of the original CHEMEQ routine (Young and Boris, 1973,1977; Young, 1980).

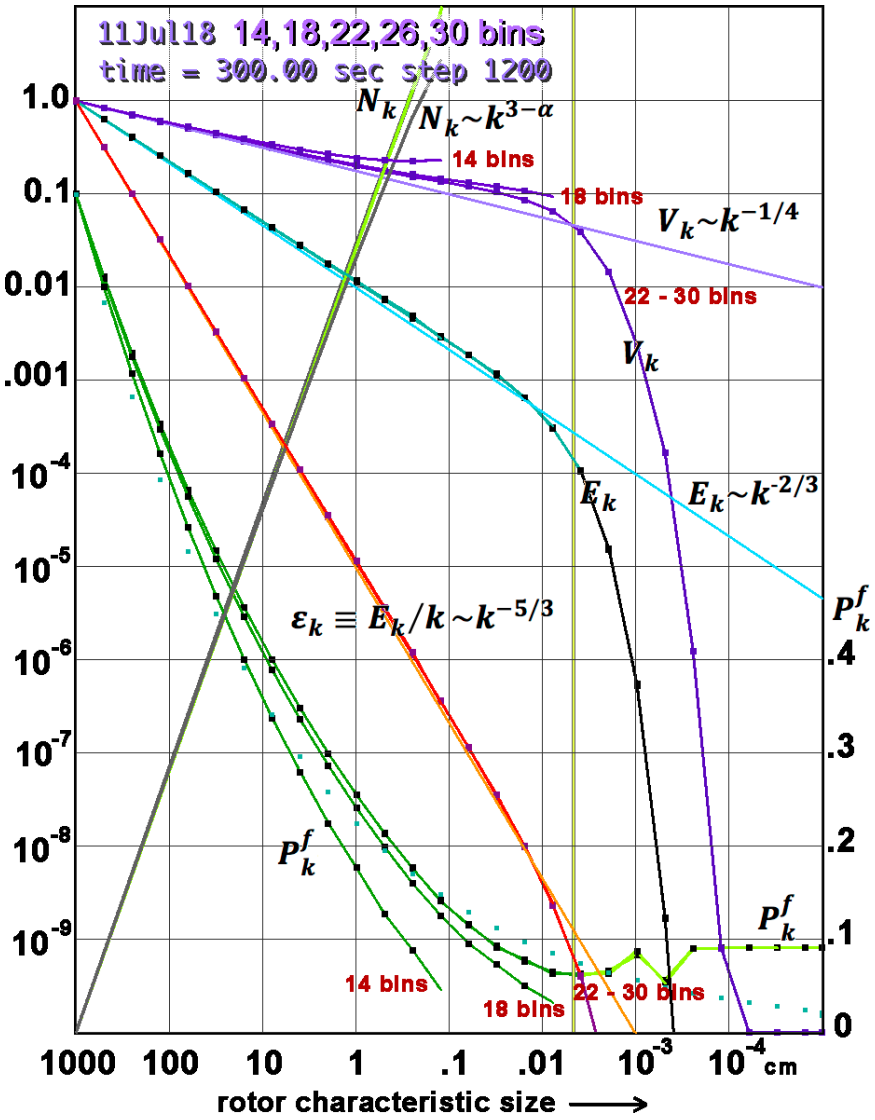

Figure 8.6. Instantaneous CSD spectrum with 14 bins, 18 bins, and 22, 26, and 30 bins displayed after 300 seconds has elapsed. The spectra resolved with 22, 26, and 30 bins have nearly identical values in common bins. Although the 18-bin solution barely reaches the dissipation zone, its larger-scale solution is quite close the converged result of the more finely resolved cases.

Figure 8.6 above and Table 8.1 below summarize several runs solving the equilibrating spectrum problem using different numbers of CSD spectral bins, specifically 14, 18, 22, 26, and 30 bins. This is a form of grid convergence appropriate to the CSD representation. These runs terminate the logarithmic spectral grid before, during, and after the dissipation scale, which can be seen to occur between bins 18 and 23 in Fig, 8.6. The program has drawn a vertical bar (black and yellow) just after bin 18 indicating where the viscous damping rate first exceeds the coherent structure interaction rate. The CSD model degrades gracefully when the spectrum is under resolved. With 22 bins, the result is nearly identical to the converged solution in Fig. 8.4 even

though the dissipation zone is truncated. Even when truncated near the beginning of the dissipation zone, as with the 18-bin case, the solution at larger scales is very close to the complete solution. The solutions with 26 bins are shown in earlier figures and the solution with 30 bins is in no demonstrable way different from the 26-bin solution. However, the solution with only 14 bins is not a useful approximation, as clearly indicated by Fig 8.6.

Table 8.1 captures some of the performance figures as a function of time during the equilibration process. Only the runs with 18 through 30 bins are included in the table and the time step was fixed at 1 second. This is the longest timestep and somewhat reduces the overall running time of the model but this may be the way CSD would be used within a larger CFD model. For the different number of bins in the scale-size grid, the cumulative number of derivative evaluations used by CHEMEQ2 is presented at each of the times and the number of derivative evaluations per step is calculated for the 20- or 40-second time intervals indicated. This table gives a coarse picture of how the integration is proceeding for each size of spectrum.

Table 8.1. CHEMEQ2 Performance as the Spectrum Equilibrates

Relax	18 bins		22 bins		26 bins		30 bins	
time (sec)	# function calls	# derivative calls/step	# function calls	# derivative calls/step	# function calls	# derivative calls/step	# function calls	# derivative calls/step
20	1697	84.9	2298	115	2303	115	2711	135.6
40	1891	9.7	2602	15.2	2521	10.9	3067	17.8
60	2071	9.0	2802	10.0	2693	8.6	3257	9.5
80	2241	8.5	2964	8.1	2919	11.3	3453	7.8
100	2417	17.3	3212	12.4	3143	11.2	3599	7.3
140	2773	8.9	3530	8.0	3545	10.1	3950	9.2
180	3035	6.6	3906	9.4	3899	8.9	4292	8.0
220	3317	7.1	4185	7.0	4211	7.8	4572	9.8
260	3645	8.2	4499	7.9	4559	8.7	4980	8.2
300	3955	7.8	4833	8.4	4891	8.3	5262	8.5

Table 8.1. Performance of CHEMEQ2 as the turbulent spectrum equilibrates during the 300-second runs. Initial non-equilibrium transients

During the first 20 timesteps all four runs require a number of extra derivative function evaluations to establish an efficient internal time step allowing adequate accuracy (about three or four figures). The number of derivative calls within each CHEMEQ2 call is larger when the number of bins is increased because the shortest scales (smallest rotor sizes) also have the stiffest equations. This trend is generally continued later in time when the time-step interval is increased from 20 to 40 integration steps. However, once the spectrum approaches its limiting form and significant adjustments are over, the number of derivative function calls per integration step becomes nearly constant regardless of the number of bins in the spectral grid. This is almost certainly because the asymptotic algorithm used for stiff equations does not gain accuracy by shortening the time step.

Using the 26-bin grid employed for Figs. 7.1 to 7.5, the external timestep was varied over four values, 1, 0.5, 0.25, and 0.1 second. Thus, CHEMEQ2 was called 300, 600, 1200, and 3000 times to reach the equilibrated spectrum after 300 seconds real time. The comparisons in Table 7.2 show timings for the calls to CHEMEQ2 and to the derivative evaluation subroutine that is called

by CHEMEQ2. The actual execution time per call to CHEMEQ2 (column 3) decreases with the timestep because the interval being integrated in each step is decreasing. The total time (last column) has increased in each case, however, because more total work is being done to obtain the solutions with higher time resolution. The total run time is seen to be almost directly proportional to the number of derivative subroutine evaluations (column 4). The integration subroutine does, however, consume between 10 and 20 microseconds per call outside of the derivative evaluation for error checking, algorithm selection, and result computations.

Table 7.2. CHEMEQ2 Execution Timing with Varying Timestep

dt	# CHEMEQ2 calls	Time per call to CHEMEQ2	# Derivative evaluations	Time per evaluation	# Deriv evals / CHEMEQ2	Run time to 300 sec
1 sec	300	117 μsec	4891	5.56 μsec	16.3	3.52×10^{-2} sec
0.5 sec	600	70.8 μsec	6254	4.78 μsec	10.4	4.25×10^{-2} sec
0.25 sec	1200	51.6 μsec	8364	5.24 μsec	7.0	6.19×10^{-2} sec
0.1 sec	3000	31.3 μsec	11999	5.59 μsec	4.0	9.39×10^{-2} sec

Table 7.2. Performance of CHEMEQ2 as the turbulent spectrum equilibrates during the 300-second runs. Initial non-equilibrium transients

Table 7.3 presents the computed rotor velocities for three different times at four different scale sizes (bins) , namely $R_k = 62.5$, cm, 1.953 cm, 0.0610 cm and 0.0019 cm, which correspond to bins 5, 10, 15, and 20 of the standard 26-bin test problem. The three comparison times are 20 seconds, 60 seconds, and 300 seconds, shown in Figs. 7.3, 7.4, and 7.5 respectively. The "correct" answer to this problem is not known but is best approximated by the most accurate solution computed, which is should be the case with the shortest timestep, 0.1 second.

Table 7.3. Convergence of Computed Rotor Velocities

time	bin	R_k	dt = 1.0 sec	dt = 0.5 sec	dt = 0.25 sec	dt = 0.1 sec
20 sec	k = 5	62.5000 cm	71.19105 cm/s	71.18890 cm/s	71.50863 cm/s	72.00640 cm/s
20 sec	10	1.9531 cm	23.59149 cm/s	24.78943 cm/s	26.03320 cm/s	27.72695 cm/s
20 sec	15	0.0610 cm	10.88231 cm/s	11.99042 cm/s	13.21630 cm/s	14.60028 cm/s
20 sec	20	0.0019 cm	0.31108 cm/s	0.36999 cm/s	0.41300 cm/s	0.44015 cm/s
60 sec	k = 5	62.5000 cm	80.53612 cm/s	84.22991 cm/s	86.40725 cm/s	88.14985 cm/s
60 sec	10	1.9531 cm	35.72012 cm/s	38.81041 cm/s	40.53890 cm/s	41.78087 cm/s
60 sec	15	0.0610 cm	18.81766 cm/s	20.97994 cm/s	22.01114 cm/s	22.82320 cm/s
60 sec	20	0.0019 cm	0.61200 cm/s	0.64492 cm/s	0.66731 cm/s	0.67674 cm/s
300 sec	k = 5	62.5000 cm	104.0118 cm/s	104.4158 cm/s	104.4352 cm/s	104.5995 cm/s
300 sec	10	1.9531 cm	50.92868 cm/s	51.23068 cm/s	51.25111 cm/s	51.35862 cm/s
300 sec	15	0.0610 cm	27.64371 cm/s	27.79647 cm/s	27.82880 cm/s	27.88997 cm/s
300 sec	20	0.0019 cm	0.75048 cm/s	0.75312 cm/s	0.75280 cm/s	0.75386 cm/s

Table 7.3. The computed rotor velocities at three times and four different scales are compared as a function of the CHEMEQ2 integration timestep dt. Comparing dt = 1.0 sec, 0.5 sec, and 0.1 sec to the run with dt = 0.1 sec, the differences are color coded as follows: clear = 2% or better, light yellow = 2 – 5%, light orange = 5 – 20%, light red = >20%.

The difference between the dt = 0.1 s solution and each of the dt = 1.0 s, 0.5 s, and 0.25 s solutions recorded in the table for the same elapsed time and bin is color coded in Table 7.3. Clear

cells indicated results that are within 2% of the dt = 0.1 s result. Light yellow shading indicates results between 2% and 5%, light orange between 5% and 20%, and light red indicates differences larger than 20%. The results for each of the three integration times are blocked together by bolder borders in the table. After 300 seconds, the turbulence spectrum has equilibrated with very little change likely but with residual small fluctuations, apparently associated with the extreme stiffness at the smallest scales. Essentially all the results of the three larger timesteps are within a percent of the dt = 0.1 s solution after 300 seconds. At 20 seconds and 60 seconds, the shorter timestep solutions are generally closer to the dt = 0.1 s solution with the biggest difference occurring where the solutions are changing most rapidly. The largest differences are generally observed in bins just before and within the dissipation zone in the period before the spectrum has equilibrated. The closer to equilibrium the turbulent spectrum is, the longer the CSD timestep can be. This would allow greater runtime efficiencies when CSD is being used wherever the CFD solution is evolving rather slowly.

The rotor velocity was chosen as the variable to compare in Table 7.3 because it also affords a look at the effect of viscous decay at short wavelength and at the relative importance of rotor velocity and scale. The bin 20 velocities, generally well down in the dissipation zone, are all small. However, when divided by the scale size R_k, which decreases faster than the velocity, the corresponding interaction rates are large. Bin 20 is well into the dissipation zone where the rotor velocities are being strongly damped. Nevertheless, the ratio of velocity to scale size is nearly 400, indicating may rotor precession/interaction times per second. Even in bin 15, which lies just before the dissipation zone in the pre-dissipation bump or bottleneck zone, this ratio is more than 450, indicating very stiff equations.

9. Discussion

Coherent Structure Dynamics (CSD) was developed to study the rapid time evolution of turbulent cascade without the need for expensive time-dependent CFD simulations. It focuses on the fluid-dynamic interactions of the coherent flow structures, called "rotors" here, that comprise turbulence. The evolution of the turbulence spectrum is simulated directly without the need to compute and post process individual 3D flow fields. The CSD representation is designed so the spectral evolution of an ensemble of turbulent flow realizations can be approximated with one fast computation. Necessarily some detail is not available in this representation. Nevertheless, behavior of the non-equilibrium evolution of turbulence can now be simulated over a range of scales far exceeding what can be studied with CFD. The Taylor-Green Vortex problem was used in Section 7 (Table 7.1 and Figure 7.1) to calibrate the free parameters in the CSD model. The resulting time-dependent system dissipation rate compares quite well quantitatively with CFD computations of the problem taking orders of magnitude more memory and time to compute. The Re ~ 1 million solution shown in Fig. 7.1 would take a number of months with a 1 million cubed effective grid on an exascale computer.

Turbulence models for use in CFD have generally treated the inertial-range below CFD resolution as if obeying a renormalizable or scale-similar equilibrium described by the Kolmogorov spectrum with a spectral energy density that scales as $k^{-5/3}$. CSD is a reduced-order computational model that computes an evolving turbulent energy spectrum from the system size down to and beyond the viscous dissipation scale. It is based on simple models of the nonlinear fluid dynamic interactions of the coherent structures "rotors" that actually comprise turbulence. These structures, also sometimes called filaments or "worms," are seen in a range of experiments and simulations. In addition to solving for the turbulent kinetic energy density as a function of scale size, CSD introduces a number density of coherent structures at each scale to account for the

fact that the relative spacing of these structures need not be the same at all scales. The spacing differences at each scale are non-dimensionalized in terms of a "packing fraction" that is related directly to the coherent structure number density as it evolves.

CSD addresses situations where changes in the driving fluid dynamics are fast and thus the resulting unresolved turbulence can be far from an equilibrium cascade because the small scales will not have time to populate or adjust. There are a number of situations where turbulence out of equilibrium may be important. For example, mixing on the molecular scale and thus chemical reactions can be significantly delayed while the short scales in the turbulent energy spectrum are being energized by an immature cascade. This has always been a primary concern in combustion research where non-equilibrium mixing actually empowers the turbulence at small scale. The CSD model was used to predict the evolution of a highly non-equilibrium initial condition spectrum in Section 8. This driven turbulence problem and the Taylor-Green vortex decay problem provided a number of checks on convergence with timestep and spectral resolution, energy conservation, and computational performance.

It is physically significant that the Kolmogorov Cascade establishes itself quickly, in a few large-scale turnover times (seconds), but the non-dimensional packing fraction takes minutes to relax to an equilibrium, non-constant dependence on rotor scale. Thus turbulence seems to "remember" information from a non-equilibrium initial condition long after the energy cascade is well established. It is also important to note that this dynamic, reduced-order CSD model predicts a pre-dissipation bump, or bottleneck, in the spectrum just before and entering the dissipation zone. Though well-established now by detailed simulations and experiments, this small deviation from Kolmogorov Cascade at the end of the inertial range was, at one time, attributed to numerical error in CFD.

The CSD model has been shown to work well, stably and efficiently. The model was constructed to reflect important fluid dynamic considerations: identical treatment of all scales from the system size down to below the viscous dissipation scale, positivity of the kinetic energy density and rotor number density, conservation of turbulent kinetic energy throughout the inertial range, viscous dissipation at all scales, and scale similarity in the interaction rates between the coherent structures (rotors). These physical requirements appear to be enough to give reasonable physical results for the implied fluid dynamic and turbulence behavior. This seems to say that fluid dynamics is a more robust process in our universe than necessarily captured by the Navier-Stokes equations.

The CSD model was not derived directly from the Navier-Stokes equations. It would be nice to be able to do this but the author has not been able to see how. Perhaps this is work for the future. It would also be instructive to generalize the model to allow for bin spacing other than a factor of two. Direct Numerical Simulation could do a better job of solving non-equilibrium problems such as the $R_e = 10^6$ example presented here – if we could do simulations with a $10^6 \times 10^6 \times 10^6$ grid. Even exascale may not get us there.

There are a number of input parameters in CSD and the interactions between all of them should be subjects for continuing research. Specifically, the number of rotors from a shredding interaction and the relative strengths of shredding and merging could be tied down more precisely by an extensive program of numerical simulation. This line of endeavor is open-ended, however, and beyond the scope of this paper. New issues arise such as how to measure the number of shred structures and even more fundamentally, when should merging or shredding of two rotors be considered to be complete to set the parameters γ and δ?

As mentioned above, the packing fraction does not approach a constant value as would be the case if all scales in the inertial range were self-similar. "Snapshots" of the flow fields at different scales will evidence identifiably different flow patterns even though there is no direct indicator of scale in the snapshot. Because of the insensitivity of the model results in the inertial range to the details below the dissipation scale, little attention has been paid to this region so the packing fraction is simply pegged to a representative small value. Clearly more work is suggested here since the packing fraction is a new feature with relatively little impact on the cascade of energy.

A major encouraging result was also noted above. This dynamic, mathematically stiff system relaxes to the Kolmogorov spectrum quickly in time and develops a definite pre-dissipative "bump" or "bottleneck." This phenomenon certainly is not arising in CSD from non-local triadic interactions, as they are not recognizably a part of this model. It also does not seem to be caused by the backscatter or inverse cascade that is included in CSD through the rotor-merging interactions. In fact, reducing the value of δ in the dissipation zone actually enhances the bottleneck bump slightly. CSD can be argued to support the simplest bottleneck explanation. Viscosity reduces the kinetic energy at each scale but does not move it along to smaller scales. As a result, reduction of the energy available at each scale in the dissipation zone below the Kolmogorov level cannot provide enough forward cascade to move the energy away from the pre-dissipation (mostly inertial) zone fast enough. In this view, the energy density therefore builds up a bit above the Kolmogorov level to enhance the cascade into the dissipation zone.

There seems to be a complicating factor. The packing fraction is getting smaller in the pre-dissipation zone but begins increasing again on entering the dissipation zone, as seen in Figure 7.5. In the bottleneck, therefore, the rotors will have their maximum relative separation near the peak of the bump entering the dissipation zone. At this scale the rotors are filling about 1/64 of the available space, which is roughly consistent with Figure 1.1. The smaller the packing fraction, for a given energy density, the larger is the rotor velocity from Eq. 3.7. In this case V_k is 8 times larger than it would be with a packing fraction near 1.0. It seems quite possible that the packing fraction minimum is therefore helping the energy cascade out of the bottleneck region to offset the blockage due to the viscosity.

The remaining areas of principal activity for CSD are:

1. Build a computationally tractable model driven by CSD to generate spatially correlated realizations of turbulent subgrid flow that can be integrated into an engineering-scale CFD model to enhance effective resolution locally by one or two orders of magnitude. It is entirely possible that an optimized version of CSD, with perhaps fewer bins than used in the examples above, could be introduced at every relevant element in an expensive finite-element model to give a time-resolved subgrid model of the local, non-equilibrium turbulent spectrum. Such a capability may provide a boost to reactive flow computations by modeling how quickly subgrid-scale mixing actually occurs. In the reactive flow case, the additional cost of this CSD modeling may not even approach the cost of the chemistry.

2. In one-way coupled systems with a single engineering CFD simulation providing the driving terms, numerous separate small-scale realizations from CSD could be used to develop, test and exercise control algorithms for small UAVs and drones in affordable ensembles of more realistic turbulent conditions.

3. Determine the source of the small numerical fluctuations seen in CHEMEQ2 as it approaches equilibrium and how to better optimize it while controlling error for these non-equilibrium turbulence problems. It appears that more than half of the integration effort, in terms of derivative evaluations is expended in integrating past these fluctuations.

3. Develop a way to restart the integrations for different, but simultaneous CFD cell conditions, by saving intermediate integration temporaries for each separate integration, to save time in restarting.

Research in the immediate future involves merging a fluid-like mixing algorithm driven by CSD to study the effects that non-equilibrium turbulence has on micro-scale (molecular) mixing. The issue here is to express a high-resolution model of multi-scale turbulent convection which has no numerical diffusion – so the mixing observed is a result of applied diffusion at the smallest resolved scale and not numerical diffusion at all larger scales. A "cookie-cutter" model is being used in which fluid convection is being simplified to shifts of columns of data in a Cartesian grid by integer numbers of cells parallel to grid axes. These shifts cause no diffusion or numerical mixing but large local gradients ae built up. The last step of this process, each timestep, is to diffuse the values in adjacent cells.

Acknowledgements:

The research leading to Coherent Structure Dynamics and these preliminary demonstrations was supported by the project on "Highly Complex Fluid Dynamics" within the ONR/NRL 6.1 basic research core program. The DoD High-Performance Computing Modernization Office supported the development of the FAST3D and FAST3D-CT Large-Eddy Simulation models that provided the empirical incentive and projected need for a non-equilibrium model like CSD. My NRL collaborators, Kailas Kailasanath, Gopal Patnaik, Keith Obenschain, Douglas Schwer, Junhui Liu, and David Mott contributed their expertise through numerous focusing conversations. Professors Elaine Oran and Carolyn Kaplan (University of Maryland), Professor Alexei Poludnenko (Texas A&M), Dr. Fernando Grinstein (Los Alamos National Laboratory), and Professor Paul Woodward (University of Minnesota) all have contributed significantly to the underpinnings of this work in the last few decades.

References:

N.A. Adams, S. Hickel and J.A. Domaradzki, "Approximate Deconvolution," Chapter 6 in **Implicit Large Eddy Simulation: Computing Turbulent Fluid Dynamics**, F.F. Grinstein, L.G. Margolin, and W.J. Rider (eds), (Cambridge University Press, New York USA, 2007).

J.P. Boris and J. M. Picone, "Beam Generated Vorticity and Convective Channel Mixing", Naval Research Laboratory Memorandum Report 4327, 17 September 1980.

J.P. Boris, F.F. Grinstein, E.S. Oran, and R.L. Kolbe, "New Insights into Large Eddy Simulation," Journal of Fluid Dynamics Research~10 (4–6): 199–228, December 1992.

By G.L. Brown and A. Roshko, "On density effects and large structure in turbulent mixing layers," J. Fluid Mech. vol. 64, part 4, pp. 775-816, 1974.

J.G. Brasseur and S. Corrsin, "Spectral Evolution of the Navier-Stokes Equations for Low Order Couplings of Fourier Modes", in Advances in Turbulence, edited by G. Compte-Bellot and J. Mathieu (Springer-Verlag, Heidelberg, 1987), 152–162.

J.G. Brasseur, "Comments on the Kolmogorov Hypothesis of Isotropy in the Small Scales", AIAA Paper 91–0230, 1991.

J.G. Brasseur and C-H. Wei, "lnterscale dynamics and local isotropy in high Reynolds number turbulence within triadic interactions," Phys. Fluids 6 (2), 842–870, February 1994.

J.R. DeBonis, "Solutions of the Taylor-Green Vortex Problem Using High-Resolution Explicit

Finite Difference Methods." NASA/TM-2013-217850, Glenn Research Center, Cleveland OH, 2013.

L.T. Diosady and S.M. Murman, "Case 3.3: Taylor-Green Vortex Evolution," Case summary for 3rd International Workshop on Higher-Order CFD Methods, Jan 3-4, 2015, Kissimmee, FL.

D. Drikakis, M. Hahn, F.F. Grinstein, and C.R. DeVore, C. Fureby, M. Liefvendahl, and D.L. Youngs, "Limiting Algorithms," Chapter 4a in **Implicit Large Eddy Simulation: Computing Turbulent Fluid Dynamics**, F.F. Grinstein, L.G. Margolin, and W.J. Rider (eds), (Cambridge University Press, New York USA, 2007).

V.N. Gamezo, A.Y. Poludnenko, E.S. Oran, F.A. Williams, "Transverse Waves Resulting from Pulsating Instability of Two-Dimensional Flames," 2014, *Combustion and Flame*, 161, 950.

G. Giangaspero, E. van der Weide, M. Svard, M.H. Carpenter and K. Mattsson, "Case C3.3: Taylor-Green vortex," Case summary for 3rd International Workshop on Higher-Order CFD Methods, Jan 3-4, 2015, Kissimmee, FL.

C.H. Gibson, "Fossil turbulence revisited", Journal of Marine Systems, 21 (1-4), 147-167, 1999, see also the draft article Carl H. Gibson, "What is turbulence, what is fossil turbulence, and which ways do they cascade?."

G.B. Goodwin and E.S. Oran, "Premixed flame stability and transition to detonation in a supersonic combustor," Combustion and Flame 197, 145–160, 2018.

F.F. Grinstein, "Vortex Dynamics and Entrainment in Rectangular Free Jets," *Journal of Fluid Mechanics*, **437** (2001): 69–101.

F.F. Grinstein, J.A. Saenz, J.C. Dolence, T.O. Masser, R.M. Rauenzahn, M.M. Francois, "Effects of operator splitting and low Mach-number correction in turbulent mixing transition simulations", Computers and Mathematics with Applications (2018), https://doi.org/10.1016/j.camwa.2018.05.008.

P.E. Hamlington, A.Y. Poludnenko, E.S. Oran, "Interactions Between Turbulence and Flames in Premixed Reacting Flows," Physics of Fluids (2011) 23, 125111.

A.J. Kajzer, J. Pozorski, and K. Szewc, "Large-eddy simulations of 3D Taylor-Green vortex: comparison of Smoothed Particle Hydrodynamics, Lattice Boltzmann and Finite Volume methods," Journal of Physics Conference Series **530**, 012019, 2014.

O.M. Knio and A.F. Ghoniem, "Numerical Study of a Three-Dimensional Vortex Method," Journal of Computational Physics 86, 75-106, 1990.

P. Moin and K. Mahesh, "DIRECT NUMERICAL SIMULATION: A Tool in Turbulence Research," Annual Review of Fluid Mechanics Vol. 30:539-578, 1998.

R.D. Moser, J. Kim, and N.N. Mansour, "Direct numerical simulation of turbulent channel flow up to Re 590," Physics of Fluids: **11-** 4:943–945, 1999.

D.R. Mott and E.S. Oran, "CHEMEQ2: A Solver for the Stiff Ordinary Differential Equations of Chemical Kinetics," Naval Research Laboratory Memorandum Report 6400--01-8553, 27 July 2001.

E.S. Oran and J.P. Boris, "Computing Turbulent Shear Flows - A Convenient Conspiracy," feature article, Computers in Physics 7(5): 523–533, 1993.

E.S. Oran and J.P. Boris, **Numerical Simulation of Reactive Flow**, 2nd edition, (Cambridge University Press, New York,2001).

D.I. Pullin and P.G. Saffman, "Vortex Dynamics in Turbulence," Ann. Rev. Fluid Mech. 1998, 30:31–51.

J.M. Picone, J.P. Boris, J.R. Greig, M. Raleigh and R.F. Fernsler, “Convective Cooling of Lightning Channels”, Journal of the Atmospheric Sciences 38(9): 2056–2062, September 1981, *also* Naval Research Laboratory Memorandum Report 4472, 14 April 1981.

J.M. Picone, J.P. Boris, J.H. Gardner, J.R. Greig, M. Raleigh, M. Lampe and R. Fernsler, “Theory of Beam Channel Hydrodynamics”, Proceedings: BEAMS ‘83 – Fifth International Conference on High-Power Particle Beams, 12–16 September 1983, San Francisco, CA, R.J. Briggs, A.J. Toepfer (eds): 378, LLNL, 1984.

A.Y. Poludnenko, “Pulsating Instability and Self-acceleration of Fast Turbulent Flames,” 2015, Physics of Fluids 27, 014106.

C.A.Z. Towery, A.Y. Poludnenko, J. Urzay, J. O’Brien, M. Ihme, P.E. Hamlington, “Spectral kinetic energy transfer in turbulent premixed flames,” Physical Review E **93**, 053115, 2016.

J.D. Woods, “Fossil turbulence,” Radio Science, Volume 4, Number 12, pp. 1365–1367, December 1969.

P.R. Woodward, D.H. Porter, I. Sytine, S.E. Anderson, A.A. Mirin, B.C. Curtis, R.H. Cohen, W.P. Dannevik, A.M. Dimits, D.E. Eliason, K.-H. Winkler, and S.W. Hodson, "Very High-Resolution Simulations of Compressible Turbulent Flows”, *Computational Fluid Dynamics, Proceedings of the Fourth UNAM Supercomputing Conference* Mexico City, June 2000, edited by E. Ramos, G. Cisneros, R. Fernandez-Flores, and A. Santillan-Gonzalez, pp. 3-15 *World Scientific* (2001).

V. Yakhot and S.A. Orszag, “Renormalization Group Analysis of Turbulence I. Basic Theory”, Journal of Scientific Computing, Vol. 1, No. 1, pp 3–51, 1986.

T.R. Young, Jr. and J.P. Boris, “A Numerical Technique for Solving Stiff Ordinary Differential Equations Associated with Reactive Flow Problems”, Naval Research Laboratory Memorandum Report 2611, July 1973.

T.R. Young, Jr. and J.P. Boris, "A Numerical Technique for Solving Ordinary Differential Equations Associated with the Chemical Kinetics of Reactive-Flow Problems." J. Physical Chemistry 81, 2424–2427, 1977.

T.R. Young, Jr., "CHEMEQ – A Subroutine for Solving Stiff Ordinary Differential Equations." NRL Memorandum Report 4091, 1980.